Cessation and reversals of large-scale structures in square Rayleigh-Bénard cells

Andrés Castillo-Castellanos, Anne Sergent, Bérengère Podvin, Maurice Rossi

Cessation and reversals of large-scale structures in square Rayleigh–Bénard cells

Andrés Castillo-Castellanos[1,2], Anne Sergent[2,3]†, Bérengère Podvin[2], and Maurice Rossi[1]

[1]Sorbonne Université, CNRS, Institut Jean Le Rond d'Alembert, F-75005, Paris, France
[2]LIMSI, CNRS, Université Paris-Saclay, F-91405 Orsay, France
[3]Sorbonne Université, UFR d'Ingénierie, F-75005, Paris, France

We consider direct numerical simulations of turbulent Rayleigh-Bénard convection inside two-dimensional square cells. For Rayleigh numbers $Ra = 10^6$ to $Ra = 5 \cdot 10^8$ and Prandtl numbers $Pr = 3$ and $Pr = 4.3$, two types of flow regimes are observed intermittently: consecutive flow reversals (CR), and extended cessations (EC). For each regime, we combine proper orthogonal decomposition (POD) and statistical tools on long-term data to characterise the dynamics of large-scale structures. For the regime CR, centrosymmetric modes are dominant and display a well-defined dynamics, while the less energetic non-centrosymmetric modes (here, two double roll modes) fluctuate randomly. For the regime EC, a non-centrosymmetric mode is dominant and the overall dynamics display a stochastic behaviour. Furthermore, an additional simplification of the dynamics is proposed based on a K-means clustering of the POD phase-space. It reduces the problem to a network dynamics of finite number of clusters. This simplified analysis captures the main features of the CR and EC dynamics. Finally, we analyse within a range of Rayleigh numbers up to turbulent flow, the relation between dynamical regimes and the POD energetic contents as well as the residence time in each cluster.

1. Introduction

A remarkable aspect of turbulent flows is the spontaneous organisation of coherent large-scale flow patterns superposed to the small-scale fluctuations. In many cases, different configurations for the large-scale flow are shown to coexist and display rapid switches from one another, for instance inside dynamo experiments and in the geomagnetic field under the form of polarity switches (Wicht *et al.* 2009; Valet *et al.* 2012; Fauve *et al.* 2017). Flow reversals are observed inside decaying and stochastically forced two-dimensional turbulence in the presence of rigid walls (Van Heijst *et al.* 2006; Molenaar *et al.* 2004). In turbulent Rayleigh-Bénard convection, this phenomenon is also observed where a large scale circulation (LSC), commonly referred to as the *wind of turbulence*, is shown to change sign intermittently (Niemela *et al.* 2001; Kadanoff 2001).

The structure of the LSC and the nature of its variations depend on the geometry of the container (Grossmann & Lohse 2003; Xi & Xia 2008*b*; van der Poel *et al.* 2011). In cylindrical cells, two kinds of reversals are identified: *(i)* a *rotation*-led reversal which corresponds to half a revolution of the LSC plane around the cylinder axis through azimuthal meandering, and *(ii)* a *cessation*-led reversal in which the existing LSC suddenly breaks down before re-organising into a different spatial direction (see, for instance, Niemela *et al.* (2001); Sreenivasan *et al.* (2002); Brown & Ahlers (2007); Xi & Xia (2008*a*,*b*)). For the latter, a double-roll mode is usually observed during the

† Email address for correspondence: anne.sergent@limsi.fr

transition. In cubic cells, the plane of the LSC tends to align to the diagonals of the cell and transitions from one another through azimuthal rotation, but little evidence of cessation-led reversals (Bai *et al.* 2016; Foroozani *et al.* 2017).

One way to focus on the cessation-led reversals by reducing the rotation of the LSC is to restrict the experimental study to slim rectangular cells (Sugiyama *et al.* 2010; Vasilev & Frick 2011; Ni *et al.* 2015). One may also consider two-dimensional direct numerical simulations (Sugiyama *et al.* 2010; Petschel *et al.* 2011; Chandra & Verma 2011, 2013; Podvin & Sergent 2015, 2017) since rotation-led reversals are not possible in such a configuration. Sugiyama *et al.* (2010) used two-dimensional simulations to identify a region in the (Ra, Pr) space in which reversal events are observed, in good agreement with experimental observations. For this range of (Ra, Pr), the flow inside a square cell is mainly composed of a large diagonal roll and two counter-rotating corner-rolls. As pointed out by (Sugiyama *et al.* 2010; Chandra & Verma 2013), during the transition in 2D reversals the LSC is temporarily replaced by a quadrupolar mode. In the following, we refer to this regime as the regime of *consecutive reversals* (CR). A second (and often overlooked) flow regime is observed intermittently inside the same range of (Ra, Pr). It is mainly composed either of two (counter-rotating) horizontally stacked rolls or two vertically stacked rolls (Podvin & Sergent 2015). In the following, we refer to this regime as the regime of of *extended cessations* (EC).

Decomposing the turbulent flow into coherent flow structures and incoherent turbulence, allows to focus on dynamically significant events (Hussain 1986). Such decomposition is usually performed either in terms of predetermined basis functions, like spatial Fourier decomposition (see, for instance, Das *et al.* (2000); Chandra & Verma (2011)), or in terms of basis functions extracted from the data, like Proper Orthogonal Decomposition (POD) (see, for instance Bailon-Cuba *et al.* (2010); Podvin & Sergent (2015, 2017)), Dynamic Mode Decomposition (DMD) (Schmid 2010; Horn & Schmid 2017), or Koopman eigenfunction analysis (Giannakis *et al.* 2018). From this perspective, the coherent structures correspond to a combination of various such modes and flow reversals result from the non-linear interactions between modes (Chandra & Verma 2011). Note that, reduced order models based on the three and five most energetic POD modes, are able to reproduce the main dynamical features of both regimes (Podvin & Sergent 2015, 2017).

Another viewpoint is based on energetic considerations. For the CR regime, the energetics of reversals were recently investigated in (Castillo-Castellanos *et al.* 2016) by using a combination of conditional sampling, time-rescaling, and ensemble averages. This technique was previously used for reversals in geomagnetic fields (Valet *et al.* 2012; Lhuillier *et al.* 2013). Using several hundred realisations of particular reversals, we followed the evolution of the global kinetic and available potential energies (Winters *et al.* 1995; Hughes *et al.* 2013), which led to the identification of a generic reversal mechanism. Consistent with the avalanche mechanism mentioned by Sreenivasan *et al.* (2002), reversals are driven by a localised accumulation of thermal energy until a threshold is met and energy is thereafter expelled as a single burst.

In the present paper, we use statistical approaches applied to the modal coefficients extracted from the POD. Contrary to (Castillo-Castellanos *et al.* 2016), these analyses may be performed not only to the CR regime, but also to the EC regime. The paper is organised as follows. Section 2 introduces the model equations, their numerical implementation and the POD approach. In section 3 we present the criterion used to separate the CR and EC regimes and introduce the data sampling for POD. The following sections explore the differences between both regimes: §4 focuses on the spatial structure of coherent modes, §5 on the their temporal evolution, while §6 and §7 introduce and

apply cluster analysis to analyse the interactions between competing modes for the CR and EC regimes, respectively. In section 8, we follow the energy contained inside different modes and the residence times in clusters as a function of Ra. This provides a simplified description of the various flow regimes observed. Finally, we summarize our results in section 9.

2. Model equations and analysis tools

2.1. *Physical configuration and governing equations*

Consider a fluid contained in a square cell, cooled at the top with constant temperature $T_{\rm top}$ and heated at the bottom with constant temperature $T_{\rm bot} > T_{\rm top}$. The flow equations are based on the Boussinesq approximation. The flow is defined by the *Rayleigh* and *Prandtl* numbers,

$$Ra \equiv \frac{g\beta H^3 \left(T_{\rm bot} - T_{\rm top}\right)}{\kappa\nu}, \qquad Pr \equiv \frac{\nu}{\kappa} \tag{2.1}$$

where g denotes gravity, H the cell height and β, κ, ν are respectively volumetric thermal expansion, thermal diffusivity and kinematic viscosity coefficients. As far as notations are concerned, variables x (resp. u) and y (resp. v) stand for the horizontal and vertical directions (resp. velocities). Coordinate vector $\boldsymbol{x} = (x, y)$ is equal to $(0, 0)$ at the cavity centre. One introduces the reduced temperature $\theta(\boldsymbol{x}, t) \equiv (T - T_0)/(T_{\rm bot} - T_{\rm top})$, with $T_0 \equiv (T_{\rm bot} + T_{\rm top})/2$. Given a field $a(\boldsymbol{x}, t)$, quantity $\overline{a}(\boldsymbol{x})$ (resp. $\sigma(a)(\boldsymbol{x})$) denotes the time averaged value (resp. standard deviation) computed using the complete long-term time series. Moreover $\langle a \rangle(t)$ stands for the volume average of $a(\boldsymbol{x}, t)$ over the fluid domain.

Based on the cell height H as characteristic length scale and $\frac{\kappa}{H} Ra^{0.5}$ as characteristic velocity scale, the dimensionless velocity $\boldsymbol{u} = (u, v)$ and reduced temperature θ satisfy the dimensionless system of equations

$$\left\{ \begin{array}{rcl} \boldsymbol{\nabla} \cdot \boldsymbol{u} & = & 0 \\ \partial_t \boldsymbol{u} + \boldsymbol{\nabla} \cdot [\boldsymbol{u} \otimes \boldsymbol{u}] & = & -\boldsymbol{\nabla} p + Pr Ra^{-0.5} \boldsymbol{\nabla}^2 \boldsymbol{u} + Pr \theta \boldsymbol{e}_y \\ \partial_t \theta + \boldsymbol{\nabla} \cdot [\boldsymbol{u} \theta] & = & Ra^{-0.5} \boldsymbol{\nabla}^2 \theta \end{array} \right. \tag{2.2}$$

A no-slip condition for the velocity field is ensured on walls. On top (resp. bottom) walls, one imposes $\theta = -0.5$ (resp. $\theta = 0.5$) while adiabaticity $\partial_x \theta = 0$ is satisfied on side-walls. From now on, all quantities are written in dimensionless form only.

For this system, we identify the following symmetry operators which leave the governing equations invariant: a reflection symmetry $\mathbb{S}_x$ with respect to the vertical axis $(x = 0)$,

$$\begin{bmatrix} u(x,y) \\ v(x,y) \\ \theta(x,y) \end{bmatrix} \xrightarrow{\mathbb{S}_x} \begin{bmatrix} -u(-x,y) \\ v(-x,y) \\ \theta(-x,y) \end{bmatrix} \tag{2.3}$$

and a reflection symmetry $\mathbb{S}_y$ with respect to the horizontal axis $(y = 0)$.

$$\begin{bmatrix} u(x,y) \\ v(x,y) \\ \theta(x,y) \end{bmatrix} \xrightarrow{\mathbb{S}_y} \begin{bmatrix} u(x,-y) \\ -v(x,-y) \\ -\theta(x,-y) \end{bmatrix} \tag{2.4}$$

The combination of both $\mathrm{R}_\pi = \mathbb{S}_x \circ \mathbb{S}_y = \mathbb{S}_y \circ \mathbb{S}_x$ represents the centrosymmetry.

$$\begin{bmatrix} u(x,y) \\ v(x,y) \\ \theta(x,y) \end{bmatrix} \xrightarrow{\mathrm{R}_\pi} \begin{bmatrix} -u(-x,-y) \\ -v(-x,-y) \\ -\theta(-x,-y) \end{bmatrix} \tag{2.5}$$

	Mode-Q	Mode-Q*	Mode-L	Mode-L*	Mode-S	Mode-S*
Symmetry R_π	S	S	S	S	AS	AS
Symmetry $\mathbb{S}_x$	S	S	AS	AS	AS	S
Symmetry $\mathbb{S}_y$	S	S	AS	AS	S	AS

TABLE 1. Definition of modes based on symmetry properties. In each case, we indicate whether the mode is symmetric (S) or antisymmetric (AS) with respect to $\mathbb{S}_x$, $\mathbb{S}_y$, and R_π presented in §2.1.

Pr	Ra	$n_x n_y$	t_s	n_e	$\overline{\mathrm{Nu}}$	%Diff.	Pr	Ra	$n_x n_y$	t_s	n_e	$\overline{\mathrm{Nu}}$	%Diff.
4.3	$1 \cdot 10^6$	512^2	4500	418	6.83	0.2	3.0	$1 \cdot 10^6$	512^2	4500	520	6.60	0.2
	$3 \cdot 10^6$	512^2	4500	248	9.09	0.4		$3 \cdot 10^6$	512^2	4500	310	8.82	0.4
	$5 \cdot 10^6$	512^2	4500	120	10.47	0.5		$5 \cdot 10^6$	512^2	4500	133	10.10	0.4
	$8 \cdot 10^6$	512^2	4500	76	12.14	0.7		$8 \cdot 10^6$	512^2	4500	22	11.60	0.7
	$1 \cdot 10^7$	512^2	9600	3	13.06	0.3		$1 \cdot 10^7$	512^2	9600	220	12.50	0.3
	$3 \cdot 10^7$	512^2	9600	22	18.29	0.2		$3 \cdot 10^7$	512^2	9600	261	17.60	0.5
	$5 \cdot 10^7$	512^2	65000	605	20.97	0.7		$5 \cdot 10^7$	512^2	65000	754	20.70	0.7
	$8 \cdot 10^7$	512^2	4500	66	23.96	2.6		$8 \cdot 10^7$	512^2	4500	75	23.79	2.5
	$1 \cdot 10^8$	1024^2	4500	56	25.77	0.2		$1 \cdot 10^8$	1024^2	4500	45	25.36	0.2
	$3 \cdot 10^8$	1024^2	4500	9	35.50	1.6		$3 \cdot 10^8$	1024^2	4500	1	35.06	1.5
	$5 \cdot 10^8$	1024^2	4500	-	41.09	2.8		$5 \cdot 10^8$	1024^2	4500	-	40.76	2.5

TABLE 2. Simulation parameters: Ra and Pr, number of grid points $n_x n_y$, simulation length t_s in convective time units and number of events n_e where A_{2D} changes sign during the simulation length. Numerical convergence of the Nusselt number: average Nusselt number and maximum relative difference between different definitions, see text.

which in addition to the identity form a symmetry group (Podvin & Sergent 2015). In this work, we extract a set of coherent modes M, each possessing particular symmetries with respect to each element $\mathbb{E}$ of the symmetry group. Each mode can be symmetric, i.e. $\mathbb{E}\mathrm{M} = \mathrm{M}$, or antisymmetric, i.e. $\mathbb{E}\mathrm{M} = -\mathrm{M}$. In keeping the naming scheme proposed by Podvin & Sergent (2017), we introduce the following notations for coherent modes: *(i)* two modes Q and Q^*, which are symmetric with respect to all the elements of the group; *(ii)* two modes L and L^*, which are symmetric with respect to R_π, but antisymmetric with respect to $\mathbb{S}_x$ and $\mathbb{S}_y$; and *(iii)* two modes S and S^*, also known as symmetry-breaking modes, which are antisymmetric with respect to R_π. However, mode S is symmetric with respect to $\mathbb{S}_y$ and antisymmetric with respect to $\mathbb{S}_x$, while mode S^* has the opposite symmetries (see table 1).

2.2. *DNS: parameter range and numerical method*

The values of (Ra, Pr) used for direct numerical simulations (DNS) covers the transition to a turbulent flow regime where reversals have been reported (Sugiyama *et al.* 2010): $Ra = 10^6 - 5 \cdot 10^8$ for $Pr = 3$ and $Pr = 4.3$. The length of the simulations range from 4500 to 60000 convective time units as to observe an adequate number of reversals of the LSC (see table 2).

Time integration of the governing equations 2.2 is performed through a second-order semi-implicit scheme. It combines a staggered in time discretisation of the velocity and scalar fields with an implicit treatment of the diffusion terms and the Bell-Colella-Glaz advection scheme (Bell *et al.* 1989) for the non-linear terms. Details of this method can

be found on (Popinet 2003, 2009). The time step is variable and verifies the Courant-Friedrichs-Lewy condition CFL < 0.5. Incompressibility is imposed by a projection method. Numerical implementation is done using Basilisk (Popinet 2015). The code has been validated and verified for Rayleigh-Bénard convection in Castillo-Castellanos *et al.* (2016). Simulations are performed using the finite volume method on a regular Cartesian centred grid with 512 or 1024 points in each direction. We verify the spatial resolution by evaluating the numerical convergence of time-averaged Nusselt numbers obtained by different methods: integrated over the top and bottom plates, over the volume, and derived from exact relations to the viscous and thermal dissipation rates (Shraiman & Siggia 1990). In general, these values converge within 2% of the average Nusselt number, see table 2.

2.3. *Mode extraction using Proper Orthogonal Decomposition (POD)*

In the following sections, we extract the coherent structures based on Proper Orthogonal Decomposition (POD). Given a data set $\boldsymbol{\psi}(\boldsymbol{x}, t)$, this procedure determines an optimal set of orthonormal spatial functions $\boldsymbol{\phi}_k(\boldsymbol{x})$ on which the fields can be decomposed

$$\boldsymbol{\psi}(\boldsymbol{x}, t) = \sum_{k=1}^{\infty} \alpha_k(t)\boldsymbol{\phi}_k(\boldsymbol{x}) \tag{2.6}$$

Function $\boldsymbol{\phi}_k(\boldsymbol{x})$ denotes a normalized eigenfunction of the spatial autocorrelation tensor $\mathbf{R}(\boldsymbol{x}, \boldsymbol{x}') \equiv \overline{\boldsymbol{\psi}(\boldsymbol{x}, t)\boldsymbol{\psi}(\boldsymbol{x}', t)}$

$$\int \mathbf{R}(\boldsymbol{x}, \boldsymbol{x}')\boldsymbol{\phi}_k(\boldsymbol{x}')\mathrm{d}\boldsymbol{x}' = \lambda_k\boldsymbol{\phi}_k(\boldsymbol{x}) \tag{2.7}$$

associated with the eigenvalue λ_k. It can be shown that the amplitudes $\alpha_k(t)$ are such that $\overline{\alpha_j\alpha_k} = \delta_{jk}\lambda_k$, δ_{jk} being the Kronecker symbol. Modes are then ordered according to their energetic content that is $\lambda_1 > \lambda_2 > \cdots \lambda_k$.

Due to the size of the physical grid ($n_x n_y \sim 10^5$), we use the snapshot method (Sirovich 1987). First one approximates the correlation tensor $\mathbf{R}$ from N individual snapshots obtained at instants t_n as

$$\mathbf{R}(\boldsymbol{x}, \boldsymbol{x}') = \frac{1}{N}\sum_{n=1}^{N} \boldsymbol{\psi}(\boldsymbol{x}, t_n)\boldsymbol{\psi}(\boldsymbol{x}', t_n) \tag{2.8}$$

Second, the eigenfunctions are assumed to be a linear combination of these N snapshots

$$\boldsymbol{\phi}_k(\boldsymbol{x}) = \sum_{n=1}^{N} \beta_k(t_n)\boldsymbol{\psi}(\boldsymbol{x}, t_n) \tag{2.9}$$

so that the eigenvalue problem 2.7 can be rewritten as

$$\mathrm{C}_{mn}\beta_k(t_n) = \lambda_k\beta_k(t_m), \text{ with } \mathrm{C}_{mn} \equiv \langle\boldsymbol{\psi}(\boldsymbol{x}, t_m)\boldsymbol{\psi}(\boldsymbol{x}, t_n)\rangle \tag{2.10}$$

leaving one eigenvalue problem of size N^2 instead of $9n_x^2n_y^2$. Moreover it can shown that $\beta_k(t_n) = \alpha_k(t_n)/\lambda_k$ (more details in (Holmes *et al.* 2012)).

For the present work, the data set is composed of joint velocity and temperature field

$$\boldsymbol{\psi}(\boldsymbol{x}, t) = (\theta, u, v). \tag{2.11}$$

As a result, the set of orthonormal functions is such that $\boldsymbol{\phi}_k = (\phi_k^\theta, \phi_k^u, \phi_k^v)$ and the

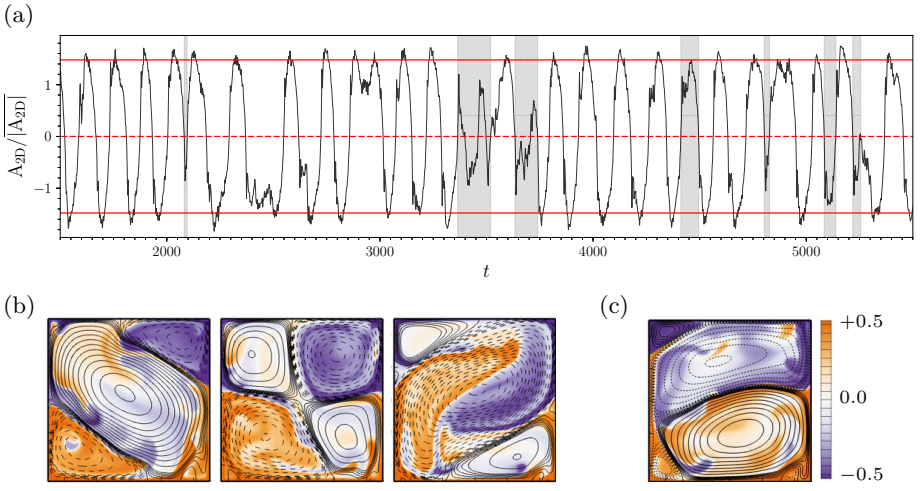

FIGURE 1. Figure (a) Time evolution of $A_{2D}(t)$ scaled by $\overline{|A_{2D}|}$ for $(Ra = 5 \cdot 10^7, Pr = 3)$. The threshold separating the CR and EC regimes set to $A_{thres} = \overline{|A_{2D}|} + \sigma(|A_{2D}|)$ is shown in red. White areas correspond to CR, while grey areas correspond to EC. Figure (b) (resp. (c)) displays snapshots taken inside the CR (resp. EC) regime. Colour indicates temperature field $\theta(\boldsymbol{x}, t)$ and lines are streamlines (negative values shown in dashed).

combined energy reads as

$$E_{comb} \equiv \langle \overline{\theta^2 + \boldsymbol{u}^2} \rangle = \sum_{k=1}^{\infty} \lambda_k \tag{2.12}$$

Our POD implementation was validated by applying it to two data sets: a first set of 1152 snapshots for $(Ra = 5 \cdot 10^7, Pr = 3)$, and a second set of 1200 snapshots for $(Ra = 5 \cdot 10^7, Pr = 4.3)$. In both cases, snapshots were taken every 5 convective time units (t.u.) from the complete series. Using a longer series or a smaller sampling time did not affect results, giving some confidence in the robustness of our mode extraction. For $(Ra = 5 \cdot 10^7, Pr = 4.3)$, results are in good agreement with published results by (Podvin & Sergent 2017): we obtain a similar set of structures, which display the same symmetries and similar energy contents (not presented here).

3. Data Processing: Identification of regimes and conditional sampling

3.1. *Identification of the two flow regimes*

For the range of (Ra, Pr) considered, two different dynamical regimes have been identified by following the global angular momentum

$$A_{2D}(t) \equiv -\frac{1}{2} \int \boldsymbol{x}^2 \omega(\boldsymbol{x}, t) \, \mathrm{d}\boldsymbol{x}, \qquad \text{with } \omega(\boldsymbol{x}, t) = \partial_x v - \partial_y u \tag{3.1}$$

as a function of time (figure 1a). Indeed, this quantity is a measure of the organised rotation around the centre of the cavity (Molenaar *et al.* 2004). A criterion based on the amplitude of A_{2D} was proposed to discriminate the two regimes (Podvin & Sergent 2015; Castillo-Castellanos *et al.* 2016). If $|A_{2D}| > A_{thres}$ (here set to $A_{thres} = \overline{|A_{2D}|} + \sigma(|A_{2D}|)$) during the interval between two consecutive sign changes in A_{2D}, then the time interval is assigned to the regime of *consecutive reversals* (CR), corresponding to white areas in

figure 1a. A time interval where such threshold is not reached can be of two kinds: weak or *rogue reversals* if only one consecutive sign change is observed, and a cessation of the LSC otherwise. For simplicity, both kinds are assigned to the regime of *extended cessations* (EC), corresponding to grey areas in figure 1a. On the one hand, consecutive reversals are characterised by alternating positive and negative plateaus in A_{2D}. Positive (resp. negative) plateaus are associated to a large counter-clockwise (resp. clockwise) diagonal roll with two corner-rolls (see figure 1b). On the other hand, extended cessations are characterised by a more erratic dynamics and by the absence of a central vortex (see figure 1c).

3.2. *Conditional sampling for POD*

Conditional sampling allows to distinguish and provide quantitative information about interesting spatial and/or temporal regions of a turbulent flow (Antonia 1981). Here, we use the aforementioned criterion to separate our data into two subsets: a first one which corresponds to the CR regime only and a second one which excludes this regime, leaving mostly the EC regime. The idea is now to apply a POD analysis to each subset separately and investigate in detail the dynamics of each regime. In the sections 4 to 7, we focus on the values $(Ra = 5 \cdot 10^7, Pr = 4.3)$ and $(Ra = 5 \cdot 10^7, Pr = 3)$ since the system displays in that two cases, an intermittency between the CR and EC regimes. For reference, at $(Ra = 5 \cdot 10^7, Pr = 4.3)$ (resp. $(Ra = 5 \cdot 10^7, Pr = 3)$) the probability of being inside the CR regime is 83.0% (resp. 79.6%) of the complete series. It is thus possible to highlight the different roles played by the large-scale modes from different viewpoints. These observations will be used in section 8 to follow the large-scale flow dynamics over a wider range of Ra numbers.

For $(Ra = 5 \cdot 10^7, Pr = 4.3)$, the CR subset is restricted to 100 flow reversals, corresponding to 3157 snapshots taken every 4 convective time units. The sampling frequency of snapshots has been adjusted to ensure the different phases of the flow reversals are represented and the number of snapshots was progressively increased until the convergence of POD modes is reached. The EC subset is composed of 3800 snapshots taken every convective time unit. The sampling frequency was increased due to the generally faster dynamics and short duration of this regime. For this regime it was more difficult to obtain converged POD modes and small differences are still observed when considering different sets of snapshots. For $(Ra = 5 \cdot 10^7, Pr = 3)$ the CR subset is composed of 108 reversals, corresponding to 1521 snapshots taken every 4 time units, while the EC subset is composed of 1500 snapshots taken every time unit.

4. Comparison of the spatial structures extracted from each regime

For $(Ra = 5 \cdot 10^7, Pr = 4.3)$ and $(Ra = 5 \cdot 10^7, Pr = 3)$ and both CR and EC subsets, the POD spectra exhibits at least two decades of decay between modes $k = 1$ and $k = 20$ (figure 2). The two first modes of the CR regime represent around 80% percent of the combined energy E_{comb}, with an additional 10% contained inside modes $k = 3$ to 6 for $Pr = 4.3$ (resp. modes $k = 3$ to 7 for $Pr = 3$). In comparison, the first two and six modes of the EC regime represent 70% and 86% of E_{comb}, respectively. Generally EC modes $k = 2$ to $k = 20$ are more energetic than their CR counterparts, indicating a stronger competition between POD modes for the EC subset. In sections 4.1 and 4.2, we study only on the six most energetic POD modes for each regime. In the following and whenever there is no ambiguity, we refer to the amplitude $\alpha_k(t)$ of the mode k as the mode itself. For instance if $k = 1$ mode is a mode Q, α_1 is written as Q.

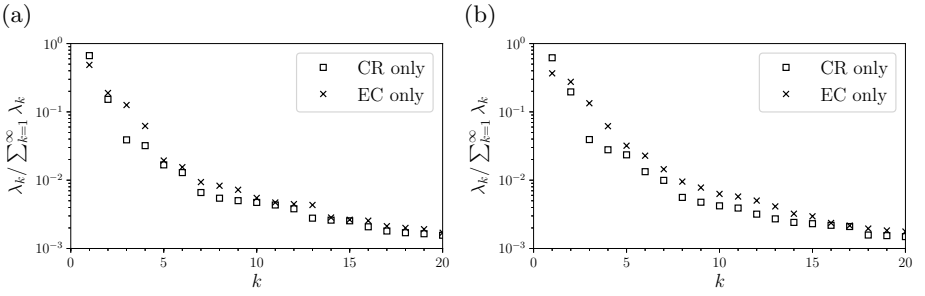

FIGURE 2. Conditional POD analysis of the CR and EC subsets. Normalised eigenvalues for the first 20 modes for $Ra = 5 \cdot 10^7$ for (a) $Pr = 4.3$ and (b) $Pr = 3.0$.

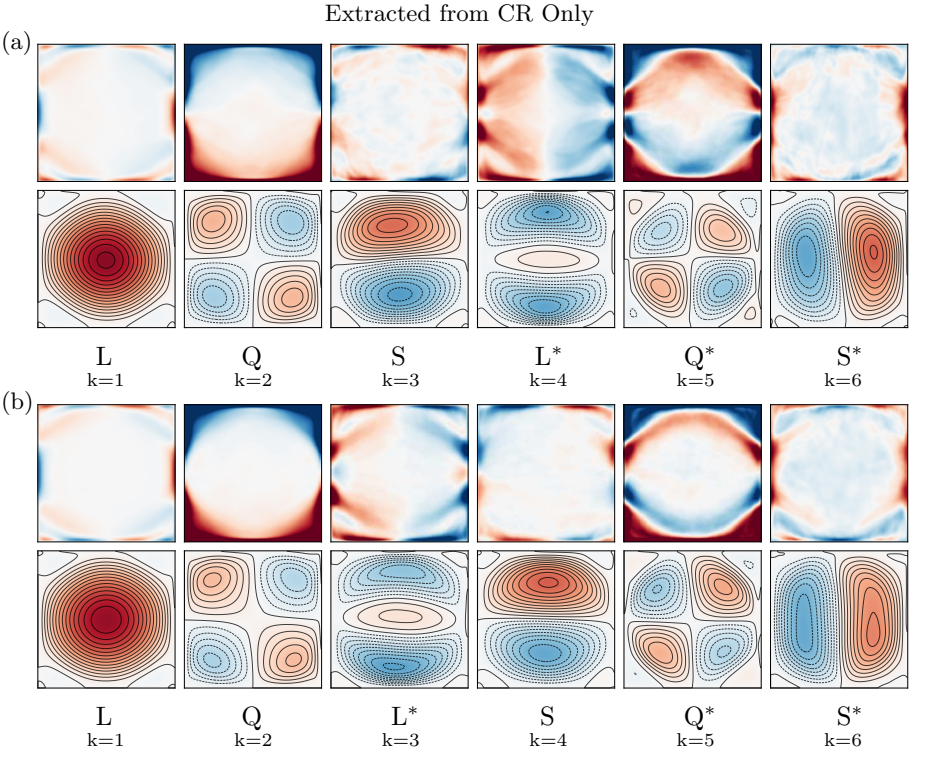

FIGURE 3. Leading POD modes of the CR subset obtained for $Ra = 5 \cdot 10^7$ and (a) $Pr = 4.3$, (b) $Pr = 3.0$. For each figure, colour corresponds to the temperature modes ϕ_k^θ (top row) and to the streamfunction of the velocity modes (ϕ_k^u, ϕ_k^v) (bottom row). Streamlines are also presented in bottom row with dashed lines for negative streamfunction values.

4.1. *Leading POD modes inside the regime of 'consecutive reversals' (CR)*

Figure 3a displays the POD modes extracted from the CR subset for ($Ra = 5{\cdot}10^7, Pr = 4.3$). Each mode displays a clear symmetry: $k = 1$ corresponds to mode L, associated to a single-roll mode with small recirculation cells in the corners; $k = 2$ corresponds to mode Q, associated to a four-roll mode and to the mean temperature field; $k = 3$ to mode S, composed of two vertically stacked rolls; $k = 4$ to mode L^*, composed of three vertically stacked rolls; $k = 5$ to mode Q^*, similar to mode Q, but with four additional rolls carrying cold (resp. hot) fluid close to the bottom (resp. top) plate; and finally $k = 6$

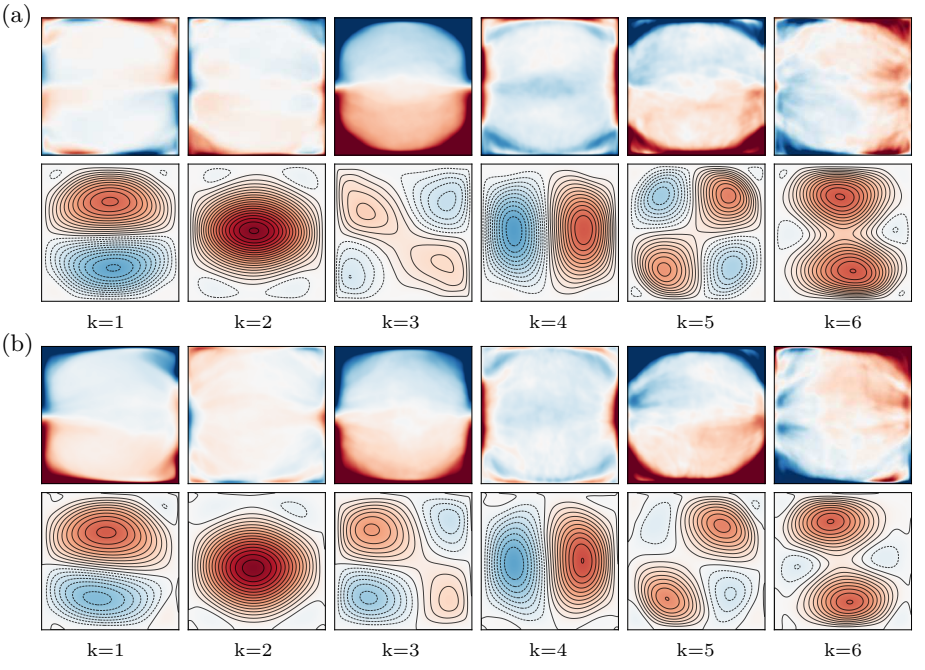

FIGURE 4. Most energetic POD modes of the EC subset obtained for $Ra = 5 \cdot 10^7$ and (a) $Pr = 4.3$, (b) $Pr = 3.0$. Temperature and velocity modes are displayed as in figure 3.

to mode S^*, composed of two horizontally stacked rolls. A similar set of POD modes is obtained for ($Ra = 5 \cdot 10^7, Pr = 3$), but modes $k = 3$ and $k = 4$, are interchanged (figure 3b). In addition, this set of modes is similar to the one extracted from the complete series (see, for instance, figure 1 from Podvin & Sergent (2017)), but with $k = 5$ and $k = 6$ interchanged. Because of this, the previous studies focused on the five most energetic modes (Podvin & Sergent 2015, 2017) did not include the mode Q^*.

4.2. *Leading POD modes inside the regime of 'extended cessations' (EC)*

Figure 4a displays POD modes extracted from the EC subset at ($Ra = 5 \cdot 10^7, Pr = 4.3$). Such modes are reminiscent of those extracted from the CR subset: $k = 1$ is similar to mode S. Mode $k = 2$ can be seen as a linear combination of mode L and mode L^* with $\mathrm{LL}^* > 0$, and corresponds to a vortex detached from the top and bottom plates (Podvin & Sergent 2017). Modes $k = 3$, $k = 4$, and $k = 5$, are reminiscent of mode Q, mode S^*, and mode Q^*, respectively, while $k = 6$ is a new mode specific to the EC regime. The latter one is composed of two co-rotating vortex surrounded by six smaller counter-rotating rolls. A similar set of POD modes is obtained for ($Ra = 5 \cdot 10^7, Pr = 3$), but the temperature field of $k = 1$ suggests this mode is a combination of mode S and mode Q (figure 4b).

Given the similarities between the modes extracted from EC and CR subsets (the sole exception being the mode $k = 6$ of the EC regime), we conclude that both subsets are accurately represented by the same set of coherent spatial structures. This suggests that differences between the CR and EC regimes concerns the time evolution of modal amplitudes. In the following sections, we hence project the complete time series into the set of modes extracted from the CR regime to compare the temporal evolution of amplitudes for both regimes.

5. Comparison of temporal evolution in the CR and EC regimes

We analyse here the temporal evolution in both regimes and focus on the coherent or stochastic nature of the dynamics of each POD mode.

5.1. *General temporal evolution and PDF of modal amplitudes*

Let us project the fields $\boldsymbol{\psi}(\boldsymbol{x}, t) = (\theta, u, v)$ into the set of POD modes extracted from the CR subset to obtain the modal amplitudes $\alpha_k(t)$. For simplicity, these amplitudes are then scaled by the common factor $1/\overline{|L|}$. Figure 5 displays their time evolution, and figure 6 their corresponding probability distribution functions (PDF). A different behaviour is observed for the CR and EC regimes.

During the CR regime (white areas), the dominant mode L alternates between positive and negative *plateaus*. Both A_{2D} (shown in green) and L are very well correlated and are considered as excellent indicators of the presence of flow reversals. As observed by Podvin & Sergent (2017), the time evolution of mode L^* is different for positive and negative values of L. Modes S and S^* display positive and negative peaks during transitions, but otherwise fluctuate around zero. Mode Q increases progressively during the plateaus and suddenly drops during transitions, while mode Q^* is centred around zero and displays the opposite behaviour. As for as PDFs are concerned, modes L and L^* display a bimodal distribution, modes S and S^*, a double exponential distribution, which are almost symmetric. On the contrary, modes Q and Q^* have skewed probability distributions. This behaviour can be explained as follows. If a set of amplitudes $M(t) \equiv \{L, L^*, Q, Q^*, S, S^*\}$ is obtained by the governing equations, then $\mathbb{S}_x M$, $\mathbb{S}_y M$, and $\mathrm{R}_\pi M$ are also data sets associated to these governing equations. Furthermore, contrary to modes Q and Q^* which are symmetric under operators $\mathbb{S}_x$, $\mathbb{S}_y$, and R_π, the modes $\{L, L^*, S, S^*\}$ are changed into their opposite by the action of at least one of these operators (see table 1). Consequently their PDFs are expected to symmetric with respect to zero. This is not completely the case in figure 6 due to limited number of records.

During the EC regime (shaded areas), the dominant mode S is characterized by positive and negative plateaus and its PDF takes the form of a symmetric bimodal distribution. This is equivalent to the evolution of mode L during the CR regime. Mode S is therefore a good marker for this regime. Mode S^* becomes more energetic than in the CR regime, but does not exhibit such clear plateaus. The time evolution of the other POD modes is also modified by the change of regime: modes $\{L, L^*\}$ are found to oscillate around zero or may display smaller positive and negative plateaus, while symmetric mode Q fluctuates around a non null positive value.

Most of the above observations are valid for both Pr. The time evolution of the POD modes is more regular and more clearly defined for $Pr = 3$ than for $Pr = 4.3$ (see figures 5a and 5b). Additionally, the PDFs of L and S during the EC regime are different for $Pr = 3$: L displays a more uniform distribution, whereas S displays a more prominent peak around zero.

For the above symmetry considerations, the PDFs of modes $\{L, L^*, S, S^*\}$ are symmetric with respect to zero. As such, these modes are prone to exhibit a reversing dynamics (see figure 5), and the dynamics of each mode is similar for its positive and negative values. By contrast, the PDFs of modes Q and Q^* are skewed: mode Q does not reverse, whereas mode Q^* does change sign, but evolves differently for its positive and negative values. Consequently, in order to characterise the temporal dynamics of each regime more precisely, we study the reversal process governing the reversing modes $\{L, L^*, S, S^*\}$.

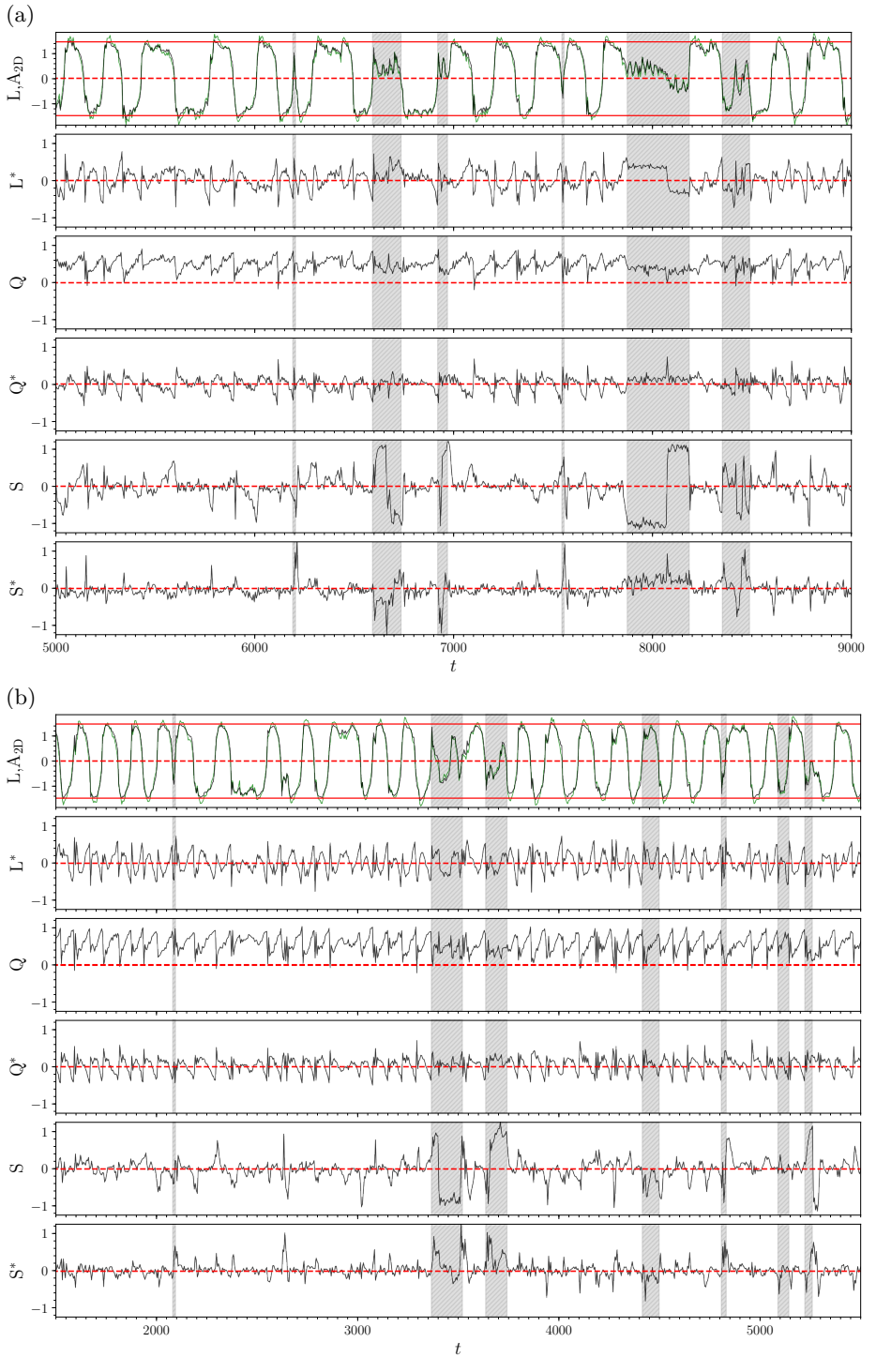

FIGURE 5. Scaled amplitudes $\alpha_k(t)/\overline{|\mathrm{L}|}$ and the scaled angular impulse $A_{2D}/\overline{|A_{2D}|}$ for (a) $Pr = 4.3$ and $Ra = 5 \cdot 10^7$, (b) $Pr = 3.0$ and $Ra = 5 \cdot 10^7$. White (resp. shaded) regions belong to the CR (resp. EC) subset. Red solid lines on the top figure pinpoints the threshold separating the CR and EC subsets.

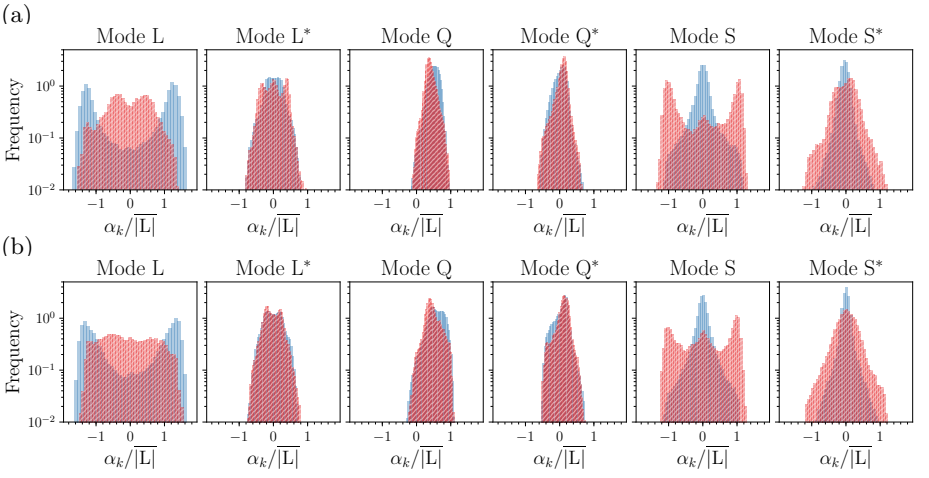

FIGURE 6. Probability distributions of the scaled amplitudes $\alpha_k(t)/\overline{|\mathrm{L}|}$ for (a) $Pr = 4.3$ and $Ra = 5 \cdot 10^7$, (b) $Pr = 3.0$ and $Ra = 5 \cdot 10^7$. PDFs inside CR regime are displayed in blue, while conditional PDFs inside EC regime are displayed in red.

5.2. *Distribution of waiting times for reversing POD modes*

To characterise the reversal process of modes $\{L, L^*, S, S^*\}$, we compute for each such mode the waiting times τ between consecutive sign changes and evaluate its probability distribution $\mathrm{P}(\tau)$. The quantity $h(\tau)\mathrm{d}\tau$ where $h(\tau) \equiv \mathrm{P}(\tau)/(1 - \int_0^\tau \mathrm{P}(\tau')\mathrm{d}\tau')$, stands for the probability of the occurrence of another reversal inside time interval $[\tau, \tau + \mathrm{d}\tau]$ where time τ is defined as the time elapsed since the last reversal. The probability distribution $\mathrm{P}(\tau)$ and $h(\tau)$ are often employed for polarity reversals of Earth's magnetic field. Polarity changes are typically assumed to originate from a general renewal process, in which reversals are independent from one another (see, for instance (Merrill *et al.* 1998; Lhuillier *et al.* 2013)). To verify whether or not the independence hypothesis is correct, the probability distribution $\mathrm{P}(\tau)$ is compared to a Gamma distribution

$$\mathrm{P}(\tau) = \left(\frac{k}{m}\right)^k \frac{\tau^{k-1}}{\Gamma(k)} \exp\left(-k\frac{\tau}{m}\right), \qquad \text{with } \Gamma(k) = \int_0^\infty x^{k-1} \exp(-x) dx \tag{5.1}$$

where $m = \overline{\tau}$ denotes the mean value of τ and the shape parameter k provides the standard deviation $m/\sqrt{k}$. For a Gamma distribution, h reaches a constant $\lim_{\tau\to\infty} h(\tau) = \frac{k}{m}$ at long time intervals (McFadden & Merrill 1986). When $k = 1$, the probability h is found always constant $h(\tau) = \frac{1}{m}$. This exponential distribution is interpreted as a lack of memory of the system: reversals are thus generated by a Poisson process characterized by an affine profile in a log plot, i.e. $\log P(\tau) = -\frac{\tau}{m} - \log m$. On the contrary, a memory effect appears when $k \neq 1$: on the one hand, for $k > 1$ the distribution is such that $\lim_{\tau\to 0} h(\tau) = 0$, indicating a temporary inhibition of future reversal events at short times. On the other hand, for $k < 1$, h diverges for $\tau \to 0$ indicating an encouragement at short times. Figure 7 (resp. 8) displays the distribution of waiting times from the CR and EC subsets for $(Ra = 5 \cdot 10^7, Pr = 4.3)$(resp. $(Ra = 5 \cdot 10^7, Pr = 3)$). PDFs are compared either to Gamma distributions with $k > 1$ (dashed lines) or to exponential distributions (solid lines) using the parameters listed in tables 3 and 4. To illustrate the goodness of each fit, tables 3 and 4 also include the quantity $\mathrm{R}^2 \equiv 1 - \sum_{bin} e^2 / \sum_{bin} \mathrm{P}^2_{\mathrm{hist}}$ where $\mathrm{P}_{\mathrm{hist}}$ is the estimated density distribution using histograms and e is the error between

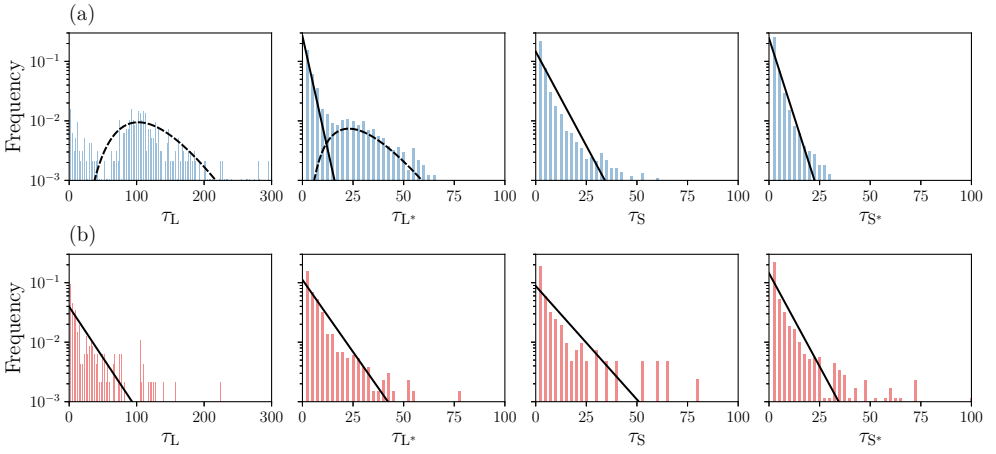

FIGURE 7. Distribution of waiting times τ_M of modes $M = \{L, L^*, S, S^*\}$ for $(Ra = 5 \cdot 10^7, Pr = 4.3)$. Figure (a) displays the CR regime and (b) the EC regime. PDFs are obtained using histograms with fixed bins of 2.5 t.u. width. Exponential (solid) and Gamma distributions with $k \neq 1$ (dashed) are drawn using parameters from table 3.

(a)

		Exp. dist.		Gamma distrib.		
τ_M	n	m	R^2	k	m	R^2
τ_L	393	-	-	7.1	119.2	0.44
$\tau_{L_*} \geqslant 11.6$	987	-	-	4.2	30.2	0.96
$\tau_{L_*} < 11.6$	3046	2.8	0.99	-	-	-
τ_S	6733	6.9	0.74	-	-	-
τ_{S_*}	10080	4.1	0.78	-	-	-

(b)

		Exp. dist.	
τ_M	n	m	R^2
τ_L	212	25.4	0.65
τ_{L_*}	706	9.0	0.82
τ_S	199	11.4	0.63
τ_{S_*}	1046	6.9	0.72

TABLE 3. (a) The CR subset for $(Ra = 5 \cdot 10^7, Pr = 4.3)$. (b) The EC subset for $(Ra = 5 \cdot 10^7, Pr = 4.3)$. Values k and m define the fit of the probability distributions of waiting times τ_M to either exponential (in that case k is set to 1) or Gamma distributions with $k \neq 1$. The coefficient R^2 quantifies the goodness of the fit (see text). Finally n denotes the number of events where a mode changes signs.

the fit and the histogram. In this context, a value $R^2 = 1$ indicates that the Gamma distribution perfectly fits the histogram.

For the EC subset, the distribution of waiting times for all reversing modes fit reasonably well to exponential distributions, so indicating a Poisson-like dynamics for all modes studied: the cessation regime seems to be composed of memoryless events. No strong indication has been found against this assertion though our records are still not long enough to provide a firm conclusion.

For the CR subset, the distributions of τ_S, and τ_{S^*} also fit well to exponential distributions. By contrast, the distributions $P(\tau_L)$ for mode L are fitted to Gamma distributions with $k = 7$ for $Pr = 4.3$ and $k = 38$ for $Pr = 3$ with a large dispersion and a peak value around $\tau_L = 100$ t.u. (resp. $\tau_L = 70$ t.u.) for $Pr = 4.3$ (resp. $Pr = 3$) which is several times larger than the large eddy turnover time $t_E \approx 3.5$ t.u. The leading mode L thus strongly deviates from Poissonian statistics, suggesting that the system keeps a form of memory of the preceding reversals. This highlights the coherent behaviour of the large-scale structures specific to the CR regime.

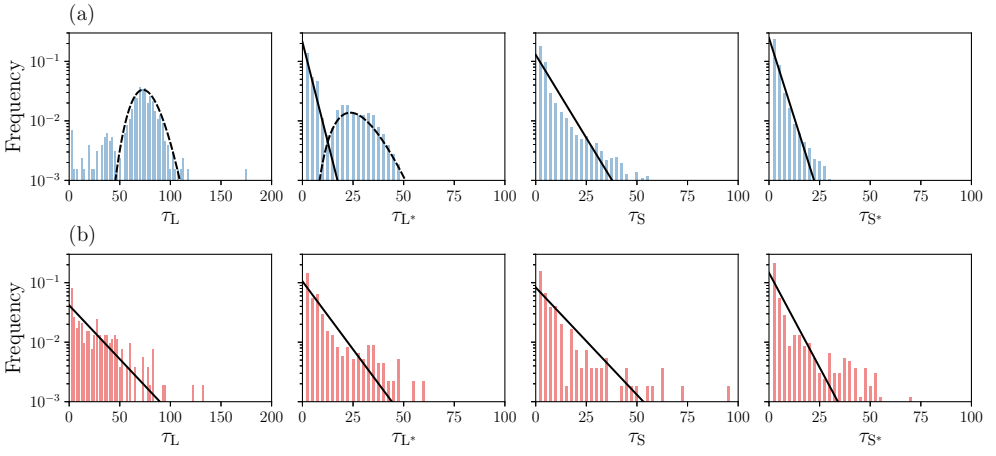

FIGURE 8. Same as figure 7 but for $(Ra = 5 \cdot 10^7, Pr = 3)$. Exponential (solid) and Gamma distributions with $k \neq 1$ (dashed) are also drawn using parameters from table 4.

(a)

		Exp. dist.		Gamma distrib.		
τ_M	n	m	R^2	k	m	R^2
τ_L	523	-	-	38.1	74.9	0.89
$\tau_{L_*} \geqslant 11.1$	1059	-	-	7.8	27.1	0.96
$\tau_{L_*} < 11.1$	2287	3.2	0.97	-	-	-
τ_S	5045	7.8	0.79	-	-	-
τ_{S_*}	8970	4.0	0.83	-	-	-

(b)

		Exp. dist.	
τ_M	n	m	R^2
τ_L	231	24.1	0.73
τ_{L_*}	675	9.5	0.83
τ_S	285	12.0	0.72
τ_{S_*}	947	6.8	0.71

TABLE 4. Same as table 3 but for $(Ra = 5 \cdot 10^7, Pr = 3)$.

The distribution of τ_{L^*} displays elements of the Exponential and Gamma distributions: if one separates the values less than a cut-off value around 11 t.u. (this value is comparable to the duration of the transition from a positive to negative plateau for A_{2D}, see (Castillo-Castellanos *et al.* 2016)). The shorter timescales $\tau_{L*} < 11$ follow an Exponential distribution, whereas the longer timescales $\tau_{L*} \geqslant 11$ are governed by a Gamma distribution with $k = 8$ for $Pr = 4.3$ (resp. $k = 9$ for $Pr = 3$).

As a final remark, evaluating the PDFs of the waiting times considering both subsets at once would mask the more coherent nature of the CR regime.

5.3. *Generic reversal in the CR regime*

The coherent behaviour in the CR regime can be further studied by revisiting the statistical approach proposed in (Castillo-Castellanos *et al.* 2016). This procedure extracts a generic reversal cycle from an ensemble of realisations. The methodology is as follows. First, the set of consecutive times t_i at which a marker R of reversal changes sign. Consider a time interval $[t_i, t_{i+1}]$ in which the marker $R \geqslant 0$; a quantity $a(t)$ in this interval is represented in the re-scaled time $t_o = (t - t_{i+1})/(t_{i+1} - t_i)$, so that $a(t_o|t_o \in [-1, 0]) = a(t|t \in [t_i, t_{i+1}])$. Similarly for an interval $[t_i, t_{i+1}]$ in which the marker $R \leqslant 0$; any quantity $a(t)$ in this interval is represented in the re-scaled time $t_o = (t - t_i)/(t_{i+1} - t_i)$, so that $a(t_o|t_o \in [0, 1]) = a(t|t \in [t_i, t_{i+1}])$. When we have a sufficiently large number of intervals $[t_i, t_{i+1}]$ of recorded flow reversals, all the

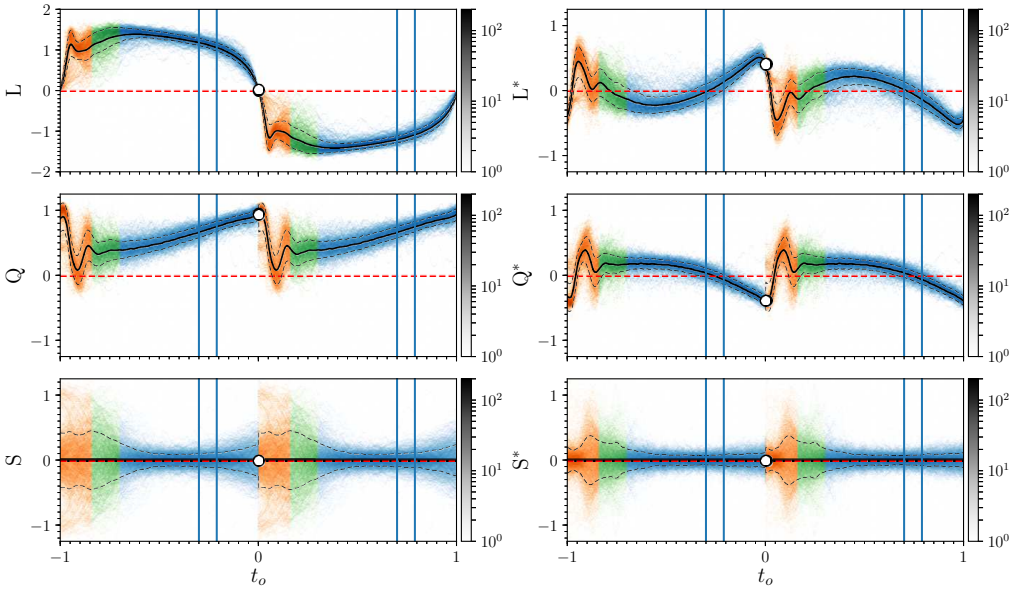

FIGURE 9. Modal amplitudes as function of re-scaled time t_o during a generic reversal for $(Ra = 5 \cdot 10^7, Pr = 3)$. Generic curves are displayed in solid lines, while dotted lines indicate one standard deviation. Colour intensity indicates the probability density, while the colour indicates the 3 phases of a generic reversal in energetic viewpoint: accumulation (blue), release (orange), and acceleration (green). A precursory region to the flow reversal is enclosed between vertical blue lines, see text.

intervals with $R \leqslant 0$ (resp. $R \geqslant 0$) are stacked together. The ensemble average over the rescaled curves represents the evolution of $a(t_o)$ during a generic reversal in the interval $t_o \in [-1, 1]$. This treatment may exhibit the presence of a dynamical path in $a(t)$ that repeats over the ensemble of realisations. When $a(t)$ displays incoherent fluctuations around zero throughout the reversal cycle, its generic curve is essentially flat, even if large fluctuations may still be observed at specific times of the generic cycle.

In (Castillo-Castellanos *et al.* 2016), the marker R of reversal was the global angular impulse $A_{2D}(t)$ while quantity $a(t)$ was the global angular impulse itself or the global kinetic energy $\mathrm{E_{kin}}(t) \equiv \int \frac{1}{2}\boldsymbol{u}^2 d\boldsymbol{x}$,or else the available potential energy $E_{apot}(t)$ (for a precise definition of $E_{apot}(t)$, see (Winters *et al.* 1995; Castillo-Castellanos *et al.* 2016)). From this energetic viewpoint, we identified a generic reversal mechanism in 3 consecutive phases. First an *accumulation* phase which is characterised by a plateau in A_{2D}, a progressive increase in E_{apot} and the growth of corner-rolls. This is followed by a *release phase* where an energy exchange from E_{apot} to $\mathrm{E_{kin}}$ is observed followed by a rebound. Finally, the *acceleration phase* corresponds to the recovery of a new stable plateau. A precursory region for release was also identified.

The same averaging procedure can be used directly on the POD mode amplitudes. This method of extracting deterministic features can be applied *a priori* to any system with a reversal without resorting to an energy analysis. Here one uses the amplitude of mode L as the marker of the reversal. For $(Ra = 5 \cdot 10^7, Pr = 3)$, the generic reversal of POD modes is presented in figure 9. For the sake of comparison with the energy analysis presented in (Castillo-Castellanos *et al.* 2016) *the accumulation* phase of E_{apot} is signalled in figure 9, by a blue colour, the *release phase* by an orange colour and the *acceleration phase* by a green colour. Finally the two vertical lines indicate the position of the precursory region.

Modes $\{S, S^*\}$ do not display any particularly coherent shape (flat generic curves with larger amplitudes observed from the precursory region until the end of the acceleration phase). By contrast, modes $\{L, L^*, Q, Q^*\}$ show some very coherent patterns. Modes $\{L, L^*\}$ carry the flow reversal. At the beginning of the accumulation phase (case with positive $L(t_o)$), L^* is negative. Due to mode spatial structures, this means effectively aiding the main circulation. During this phase, L^* increases progressively and changes sign. This dynamics weakens the flow along the upper and lower boundary layers. Note that, a peak in $L^* > 0$ coincides with the change in sign of mode L. This is followed by a sudden drop in L^*, before returning to the initial configuration where L and L^* have opposite signs. Mode Q increases progressively during the plateau state, then suddenly drops, before returning to its initial value. This is reminiscent of the generic reversal of E_{apot}. This could be expected: by construction, the contribution to E_{apot} from modes antisymmetric with respect to $\mathbb{S}_x$ is null thus leaving symmetric modes $\{Q, Q^*\}$ as the main carriers of E_{apot} since S^* is negligible. It can be shown by computation that contributions to E_{apot} from the spatial eigenfunction related to mode Q or Q^* is positive. This can be understood in terms of thermal stratification, see figure 3. As a function of time, mode Q^* is centred around zero and is anti-correlated to Q: during the generic cycle, the contribution to E_{apot} of Q^* compensates in part that of Q. Finally note that modes L^* and Q^*, change signs closely to the precursory region. Our observations place the precursory time at around 75% of t_o (or 56 t.u.). By switching signs, these modes, because of their spatial structure, mark the detachment of the LSC from the top/bottom plates and the progressive redistribution of thermal energy towards the bulk.

For the case ($Ra = 5 \cdot 10^7, Pr = 4.3$), similar trends are found. The change in sign of modes L^* and Q^* is observed around 72% of t_o (or 89 t.u.). The most noticeable difference with respect to $Pr = 3$ is a less intense rebound during the release phase. Our observations are also in good agreement with the limit cycle obtained from the 5-mode model by Podvin & Sergent (2017). The precursor event and the precursor duration as defined in the same work are also recovered in the generic cycle of POD modes.

6. Exploring the CR regime using the cluster-based analysis

One way to explore further the differences between CR and EC regimes, is to study the statistical correlations between modes. An adequate sampling frequency δt and a large number of records are key to obtain correct results. For the present work, the POD amplitudes $\alpha_k(t)$ are taken every $\delta t = 0.05$ time units. Additionally, we apply the operators $\mathbb{S}_x$, $\mathbb{S}_y$, and R_π (defined in equations 2.3 to 2.5) to the amplitudes α_k to increase the number of records since such data set is a possible one for the dynamics. This greatly facilitates the interpretation by enforcing the natural symmetries of the system.

It is not an easy matter to exhibit connections between the complete set of modes at the same time. To overcome this difficulty, we simplify further the system description: we reduce the dimensionality of the problem first by using the six more energetic POD modes only and second by applying in this 6-D subspace, a cluster-based approach proposed by (Kaiser *et al.* 2014) which reduces the phase space to a finite number K of spatial patterns. The temporal dynamics is then reduced to two elements: the trajectories followed between these clusters in this K points network and the time spent inside each cluster. Cluster analysis of the POD subspace has been previously used to study spatial and temporal intermittency in a variety of systems (for instance see Kaiser *et al.* (2014); Cao *et al.* (2014)).

6.1. *Cluster partitioning of the 6-D subspace of modal amplitudes*

This method consists in partitioning a set of 6-dimensional data points (POD amplitudes), into a finite set of K clusters. Each cluster c_k of points, is characterised by a representative state given by the cluster centroid $\boldsymbol{\mu}_k$ which is the average of the ensemble of points in c_k. The objective is to provide a drastically simplified description of the spatio-temporal dynamics in terms of finite network dynamics. The K spatial structures in terms of typical flow patterns are associated to each centroid point. For this work, the cluster partitioning is performed *via* the K-means algorithm (see, for instance Jain (2010)) as implemented by the *scikit-learn* Python package (Pedregosa *et al.* 2011). Given a number K of clusters, the K-means algorithm is tasked to find a Voronoi partition of a set of data points so that the sum of the squared error between the centroid of a cluster, and its associated points

$$\hat{J}(c_1, .., c_K) = \sum_{k=1}^{K} \sum_{\boldsymbol{\alpha}' \in c_k} \|\boldsymbol{\alpha}' - \boldsymbol{\mu}_k\|^2 \qquad \text{with } \boldsymbol{\alpha}' = (\alpha'_1, \alpha'_2, \cdots, \alpha'_6) \tag{6.1}$$

is minimized over all sets of K clusters. The minimum squared error is denoted by $J(K)$. Starting from an initial guess of the cluster centroids $\boldsymbol{\mu}_k^{i=0}$ obtained using *k-means++* (Arthur & Vassilvitskii 2007), one applies an iterative procedure. At step n of this procedure, one obtains a given value $\boldsymbol{\mu}_k^{i=n}$ and performs two actions: one builds a new Voronoi partition based on $\boldsymbol{\mu}_k^{i=n}$, thereafter new centroids $\boldsymbol{\mu}_k^{i=n+1}$ are computed using the mean values of all the points of the new partition clusters. Steps are repeated until the current and subsequent centroids converge. In the following and whenever there is no ambiguity, we use the following notation: we refer to the cluster c_k corresponding to the centroid μ_k by the centroid μ_k itself. Because of the discrete flow symmetries $\{\mathbb{S}_x, \mathbb{S}_y, \mathrm{R}_\pi\}$, each cluster is *a priori* bound to be included in one of three possible groups: *(i)* groups of 4 clusters, where none of the elements of the group satisfy a particular symmetry but each element is transformed into another member of the group by the action of $\mathbb{S}_x$, $\mathbb{S}_y$, or R_π; *(ii)* groups of 2 clusters, where each element of the group is invariant by the action of one of the symmetries among the set $\{\mathbb{S}_x, \mathbb{S}_y, \mathrm{R}_\pi\}$ and is transformed into another member of the group by the remaining symmetries; and *(iii)* groups of a single cluster, which is invariant by the action of $\{\mathbb{S}_x, \mathbb{S}_y, \mathrm{R}_\pi\}$. However, since the K-means algorithm is not constrained by symmetry, it sometimes leads to an optimum set of K clusters which does not verify the symmetry rules. If this is the case, we disregard this result.

Since $J(K)$ always decreases as we increase K, one is required to fix the number K of clusters. This choice can be done based on the decrease of the minimum squared error $J(K)$ with respect to K (like in figure 10 for instance). In our case, we also take advantage of the symmetric nature of the POD subspace to guide the choice of K. An adequate number of clusters K results from a good compromise between a small number of clusters, the decrease in the squared error $J(K)$, and also on the condition that the computed clusters verify the required symmetry rules.

6.2. *Flow patterns associated to cluster centroids in the CR regime*

For $(Ra = 5 \cdot 10^7, Pr = 3)$ the partitioning the CR subset using $K = 12$ is satisfactory: this choice results in a decrease in the squared error by more than 90% with respect to the case with $K = 1$ (figure 10a). The $K = 12$ clusters have organized in 5 groups $(G_k^{cr}, k = 1, ..., 5)$, a different colour being associated with each group:

- Three groups G_k^{cr}, $(k = 1, 2, 3)$, each characterized by two clusters which are $\mathbb{S}_x$ and $\mathbb{S}_y$ antisymmetric. The cluster centroids are denoted $\{\mu_k^+, \mu_k^-\}$, superscripts indicating the sign in mode L. Colours are green, yellow and blue, respectively.

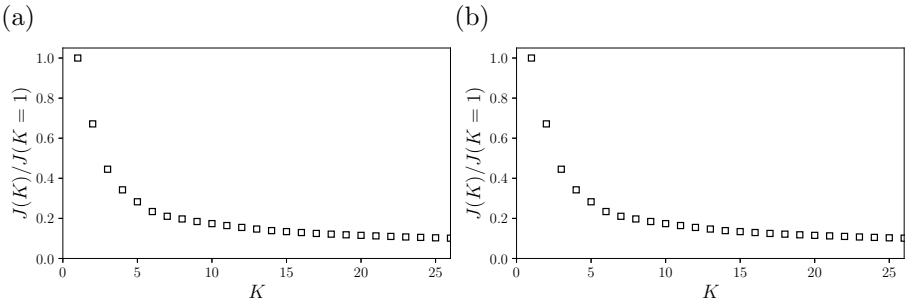

FIGURE 10. Normalised squared error $J(K)/J(K=1)$ as function of the number of clusters K for $(Ra = 5 \cdot 10^7, Pr = 3)$ inside the (a) CR regime, and (b) EC regime.

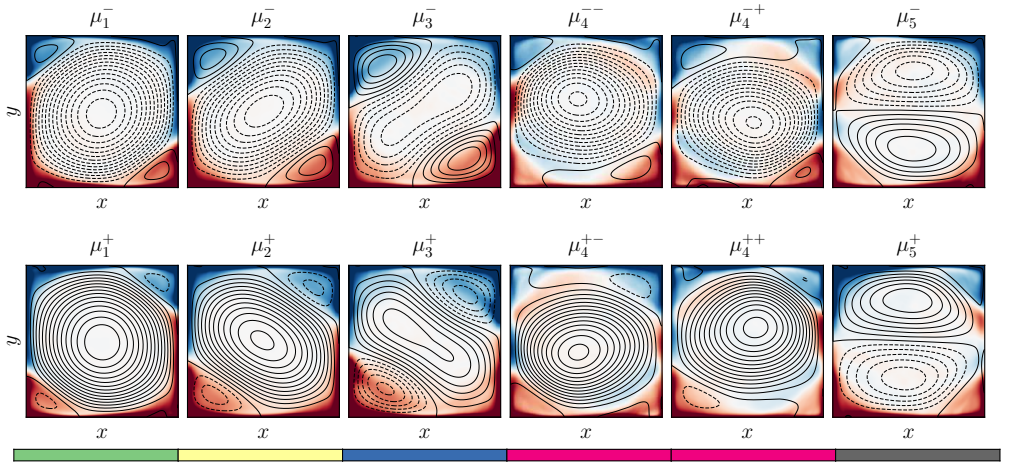

FIGURE 11. Flow patterns corresponding to the $K = 12$ cluster centroids extracted from the CR subset for $(Ra = 5 \cdot 10^7, Pr = 3)$. Colour indicates the temperature field, and lines correspond to the streamlines (negative values of streamfunction are in dashed). The five groups are identified by a different colour of the bottom ruler.

- A single group G_4^{cr} with four clusters. Centroids are denoted $\{\mu_4^{++}, \mu_4^{+-}, \mu_4^{-+}, \mu_4^{--}\}$, superscripts indicating the quadrant in the (L,S) plane. Colour is red.
- A single group G_5^{cr} with two clusters which are $\mathbb{S}_y$-symmetric. The cluster centroids are denoted $\{\mu_5^+, \mu_5^-\}$, superscripts indicating the sign in mode S. Colour is grey.

The flow patterns associated to each cluster centroid are displayed in figure 11. They indeed capture the underlying physics. For members of groups G_1^{cr} (green), G_2^{cr} (yellow) and G_3^{cr} (blue), flow patterns exhibit a large diagonal roll with counter-rotating corner-rolls of different sizes typical of the growth of corner-rolls. For members of G_4^{cr} (red) the flow pattern exhibits a central vortex partially detached from the top/bottom plates which is typical of the rearrangement of the LSC (see, for instance fields of a generic reversal presented in figure 7 in Castillo-Castellanos *et al.* (2016)). For members of G_5^{cr} (grey), the flow pattern corresponds to a vertically stacked double-roll which forms an horizontal jet. The horizontal jet impacts one of the side-walls along which two small corner-rolls are placed. This pattern is predominantly observed during extended cessations(Podvin & Sergent 2015) or just leaving this regime (see below figure 12).

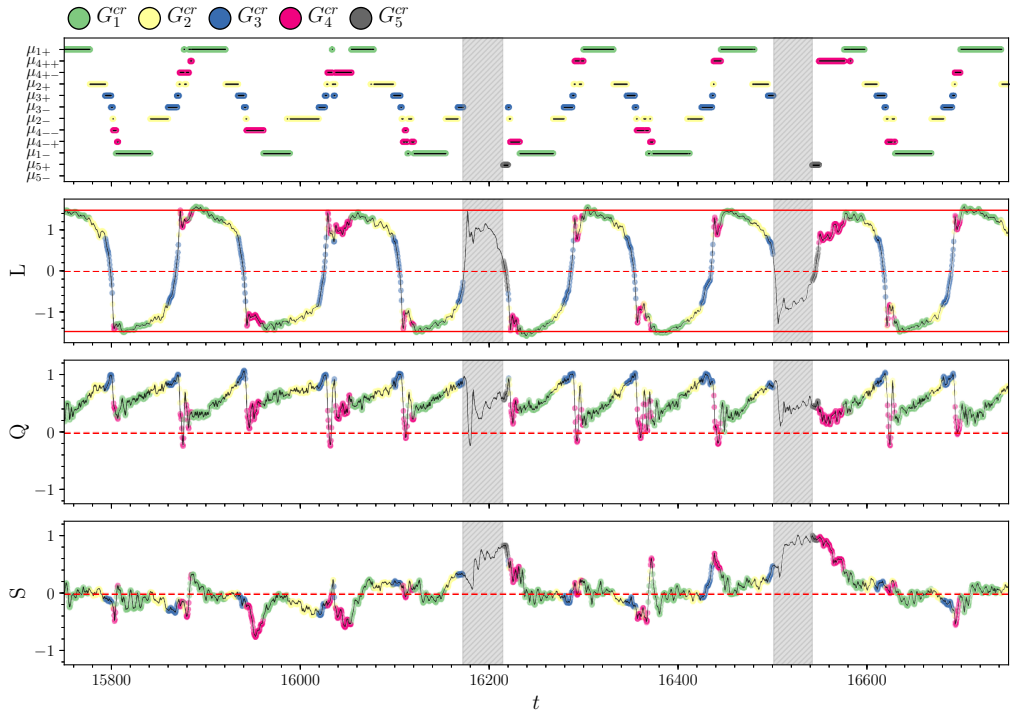

FIGURE 12. Time series of the cluster μ_k visited at time t and the corresponding amplitudes of modes L, Q, and S, during a series of particular flow reversals observed for ($Ra = 5{\cdot}10^7$, $Pr = 3$). Data-points inside the EC subset correspond to the shaded areas, whereas data-points from the CR subset are coloured to match the groups G_k^{cr}, see colour code at the top part of the figure.

6.3. *Analysis of reversals in cluster space*

The simplified representation *via clusters* is also capable to get back the three phases of the reversal cycle (accumulation, release, and acceleration). Figure 12 displays the clusters visited as a function of time are shown alongside a time series of the amplitudes of modes L, Q, and S. The time series covers a series of standard flow reversals interspersed by two weak or 'rogue' reversals, which are assigned to the EC subset and will be discussed in §7. For all standard reversals, the clusters are almost always visited in the same sequence. Starting from a positive L, the sequence $(\mu_1^+, \mu_2^+, \mu_3^+)$ illustrates the growing corner-rolls observed during the accumulation phase, where μ_2^+ roughly corresponds to a precursory region identified in §5.3. This is followed by a sequence $(\mu_3^+, \mu_3^-, \mu_2^-)$ which splits into two branches (either μ_4^{--} or μ_4^{-+}) and corresponds to the the beginning of the release phase (sign change in L) leading to the rebound event. Finally, during the complex re-organisation process typical of the acceleration phase, the system alternates between different clusters (μ_4^{--}, μ_1^-, μ_4^{-+}), before eventually settling down on μ_1^-.

Figure 13 displays in the planes (L, Q) and (L, S): (i) a random sample of data-points coloured according to the corresponding cluster groups, (ii) the position of the cluster centroids, (iii) the generic reversal cycle from §5.3. In these planes, all of cluster centroids, are located along the generic cycle with the exception of centroids $\{\mu_5^+, \mu_5^-\}$ and centroids $\{\mu_4^{++}, \mu_4^{+-}, \mu_4^{-+}, \mu_4^{--}\}$. It is inside the (L, S) plane that the two branches leading to the rebound event are best seen. Since both branches have equal probability of occurrence, by averaging over the ensemble of realisations, the generic cycle inevitably 'smoothes out'

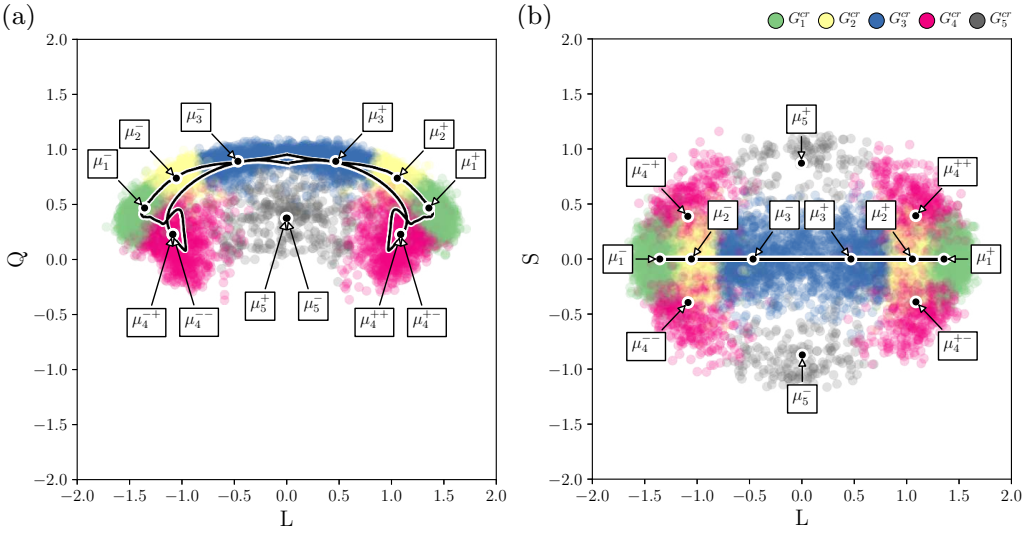

FIGURE 13. Phase diagram in the (L, Q) and (L, S) planes for $(Ra = 5 \cdot 10^7, Pr = 3)$ inside the CR subset. For reference, the generic reversal from §5.3 is displayed in solid lines. Data-points are coloured to match the groups G_k^{cr}, see colour code at the top of the figure. Solid marks indicate the corresponding centroids.

(a)

	$\%p_{cr}$	$E[\lvert A_{2D}\rvert]$	$E[\mathrm{E_{kin}}]$	$E[\mathrm{E_{apot}}]$
G_1^{cr}	43.5	1.49	1.15	0.96
G_2^{cr}	26.0	0.99	0.95	1.04
G_3^{cr}	13.6	0.36	0.76	1.09
G_4^{cr}	14.5	0.99	1.05	0.91
G_5^{cr}	2.4	0.36	0.82	1.06
	100.0	1.11	1.03	0.99

(b)

	$\%p_{ec}$	$E[\lvert A_{2D}\rvert]$	$E[\mathrm{E_{kin}}]$	$E[\mathrm{E_{apot}}]$
G_1^{ec}	21.9	1.03	1.02	0.97
G_2^{ec}	5.8	0.28	0.75	1.06
G_3^{ec}	4.6	0.31	1.03	0.84
G_4^{ec}	49.0	0.57	0.88	1.02
G_5^{ec}	18.7	0.18	0.78	1.14
	100.0	0.57	0.89	1.03

TABLE 5. Conditional averages over each of the groups extracted from the (a) CR and (b) EC regimes for $(Ra = 5 \cdot 10^7, Pr = 3)$. p_{cr} (resp. p_{ec}) denotes the probability for the system to be inside G_k^{cr} (resp. G_k^{ec}) while $E[a]$ denotes the conditional average of $a(t)$ over a cluster normalised by the average $\overline{a}$ over the complete series.

both branches. Consequently, cluster analysis is better suited to work whenever multiple transition paths are observed.

For each group G_k^{cr}, we compute the residence time $\%p_{cr}$, as well as the conditional average for different global quantities (table 5a). The system spends 70% of time inside G_1^{cr} and G_2^{cr}, while it spends 14% of time inside G_3^{cr} and G_4^{cr} each. This is in good agreement with the duration of each phase of the generic reversal cycle with an energetical viewpoint (Castillo-Castellanos *et al.* 2016). The sequences described above are also consistent with the evolution of A_{2D}, $\mathrm{E_{kin}}$, and E_{apot} during a generic reversal (not shown in the present paper). For instance, the sequence $(\mu_1^+, \mu_2^+, \mu_3^+)$ displays a gradual increase of $E[E_{apot}]$ as in the accumulation phase. The group G_5^{cr} is instead only visited whenever deviations from standard reversals become important, like at the beginning and at the end of a series of consecutive reversals (see, for instance $t \sim 16200$ and $t \sim 16550$ in figure 12). For such events the residence time is always of a few per cent (table 5a).

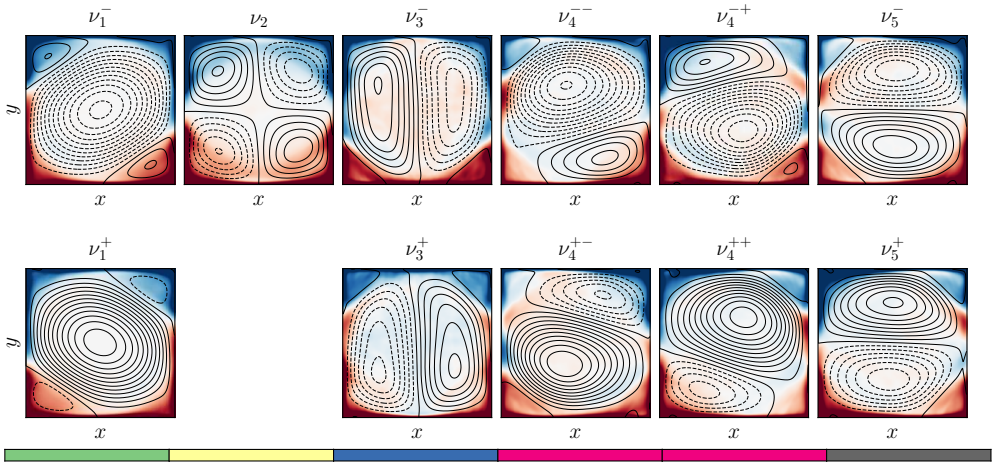

FIGURE 14. Flow patterns corresponding to the 11 cluster centroids extracted from the EC subset for $(Ra = 5 \cdot 10^7, Pr = 3)$. Colour indicates the temperature field, while lines correspond to streamlines (negative values of streamfunction in dashed). The 5 groups of centroids are identified by a different colour as shown at the bottom ruler of the figure.

7. Exploring the EC regime using the cluster-based analysis

In the previous section, we have shown that cluster analysis recovers the features of the CR regime obtained using the statistical method of section 5.3 and it is even able to obtain more detailed aspects. Here, the same cluster analysis explores the regime of extended cessations (EC), which is a regime far less well understood. Note that the statistical method used in section 5.3 would be ineffective for EC.

7.1. *Flow patterns associated to the cluster centroids in the EC regime*

Partitioning the EC subset using $K = 11$ clusters results in a decrease in the squared error by more than 80% with respect to the case $K = 1$ (figure 10b). The centroids extracted from the EC subset are noted ν_k in order to differentiate the CR and EC subsets. For $K = 11$, we have identified 5 groups of cluster (a different colour is used for each group)

- A single group G_1^{ec} with two clusters which are $\mathbb{S}_x$ and $\mathbb{S}_y$ antisymmetric. Centroids are denoted $\{\nu_1^+, \nu_1^-\}$, superscripts indicating the sign of mode L. Colour is green.
- A single group G_2^{ec} with a single cluster $\{\nu_2\}$ which satisfies all the symmetries. Colour is yellow.
- A single group G_3^{ec} with two clusters which are $\mathbb{S}_x$-symmetric. The cluster centroids are denoted $\{\nu_3^+, \nu_3^-\}$, superscripts indicating the sign of mode S*. Colour is blue.
- A single group G_4^{ec} with four clusters. Centroids are denoted $\{\nu_4^{++}, \nu_4^{+-}, \nu_4^{-+}, \nu_4^{--}\}$, superscripts indicating quadrant in the (L,S) plane. Colour is red.
- A single group G_5^{ec} with two clusters which are $\mathbb{S}_y$-symmetric. The cluster centroids are denoted $\{\nu_5^+, \nu_5^-\}$, superscripts indicating the sign of mode S. Colour is grey.

The flow patterns associated to each centroid are shown in figure 14. The large diagonal rolls are associated to ν_1^+ and ν_1^- while the quadrupolar mode associated to ν_2 is commonly observed during standard reversals in the CR regime. For ν_3^+ and ν_3^-, the flow pattern is a horizontally stacked double-roll with small corner-rolls along the top or bottom plates. For $\{\nu_4^{++}, \nu_4^{+-}, \nu_4^{-+}, \nu_4^{--}\}$ the flow pattern corresponds to a large vortex squeezed between one small and one big corner-roll, clearly reminiscent to that of $\{\mu_4^{++}, \mu_4^{+-}, \mu_4^{-+}, \mu_4^{--}\}$. For ν_5^+ and ν_5^-, the flow pattern corresponds to a vertically

stacked double-roll with corner-rolls along the left or right side-walls, which is nearly identical to that of μ_5^+ and μ_5^- from the CR subset.

7.2. *A cluster space approach of cessations*

The use of a cluster-based analysis in POD subspace allows to study the EC regime. For instance, one may analyse the clusters visited as a function of time as presented in figure 15, alongside a time series of modes L, Q, and S. Cessation dynamics could also be analysed using phase diagrams in the (L, S) and (S, S^*) planes. This is performed on figure 16 which includes a random sample of data-points coloured according to the corresponding cluster groups and the position of the cluster centroids.

First, note that data-points in figure 16 are evenly distributed between the clusters inside groups G_1^{ec}, G_4^{ec}, and G_5^{ec}. This is confirmed by computing the residence time for each *single* cluster, which is at most 12% and is consistent with table 5b since the residence time $\%p_{ec}$ in each group is nearly proportional to the number of elements.

The cluster-based analysis discriminates between different kinds of dynamical events within EC regime. Based on the sequence of clusters visited, ones identifies two dynamics: 'rogue' reversals (windows in figure 15 containing $t \sim 8800$ and $t \sim 9300$) and actual cessations of the LSC (the remaining windows). Rogue reversals deviate from standard reversals in CR mainly because of a larger amplitude of mode S. This is likely due to the asymmetric growth of corner-rolls. During these events, data-points are found to visit prominently the cluster group G_1^{ec} and to a smaller degree the group G_4^{ec}. At the beginning of each rogue reversal, the system visits G_2^{ec}, then G_1^{ec}, It may then visit G_4^{ec} and G_1^{ec} through different paths.

At the beginning of every actual cessation, the system visits G_2^{ec}, then G_1^{ec} as for rogue reversal. However the situation is then dynamically quite different: mode L oscillates around zero, mode Q fluctuates around a nearly constant value and mode S displays a plateau sporadically interrupted by short excursions like the ones observed around $t \sim 8600$, $t \sim 9100$, and $t \sim 9900$ in figure 15. On the (L, S) and (S, S^*) planes, clusters $\{\nu_4^{-+}, \nu_5^+, \nu_4^{++}\}$ and $\{\nu_4^{--}, \nu_5^-, \nu_4^{-+}\}$ are found to be sufficiently close to one another to be considered as part of two attractive basins. This qualitative assessment can be confirmed by measuring the distance between centroids in the 6-D subspace. These basins precisely correspond to the actual cessations (plateau in mode S, oscillation in L). In trajectory terms, the system moves back and forth between three clusters inside the groups G_4^{ec} and G_5^{ec}, e.g. $\{\nu_4^{-+}, \nu_5^+, \nu_4^{++}\}$ and the short excursion of mode S are through G_1^{ec}, G_2^{ec}, and G_3^{ec} before returning to one of the attractive basins. From the centroid patterns of figures 14, it can be inferred that the back and forth between G_4^{ec} and G_5^{ec} is related to the competition between two counter-rotating vertically stacked vortices, where the relative size is reflected on the sign of L. This is observed in the snapshots presented in figures 17a to 17f. Oscillations in mode L are physically related to a continuous push and shove motion between a large ascending plume and one descending along one of the side-walls from which an horizontal jet is formed. Both plumes remain locked along the same side-wall until the plateau in mode S is disrupted during a short excursion. A short excursion is presented in figures 17g to 17l. This particular event is triggered by the weakening of the horizontal jet (figure 17g) which favours the emergence of a quadrupolar pattern (figure 17h). A new unstable pattern forms from the merging of vortices coming from opposite corners (figure 17i). This new flow structure rotates until it eventually re-organises into a more stable vertically stacked double-roll pattern. The most commonly observed feature during the rotation of the unstable pattern is the brief passage of an intense plume through the centre of the cavity, which corresponds to the passage through G_3^{ec} (figure 17j). This rapid event is characterised by large fluctuations

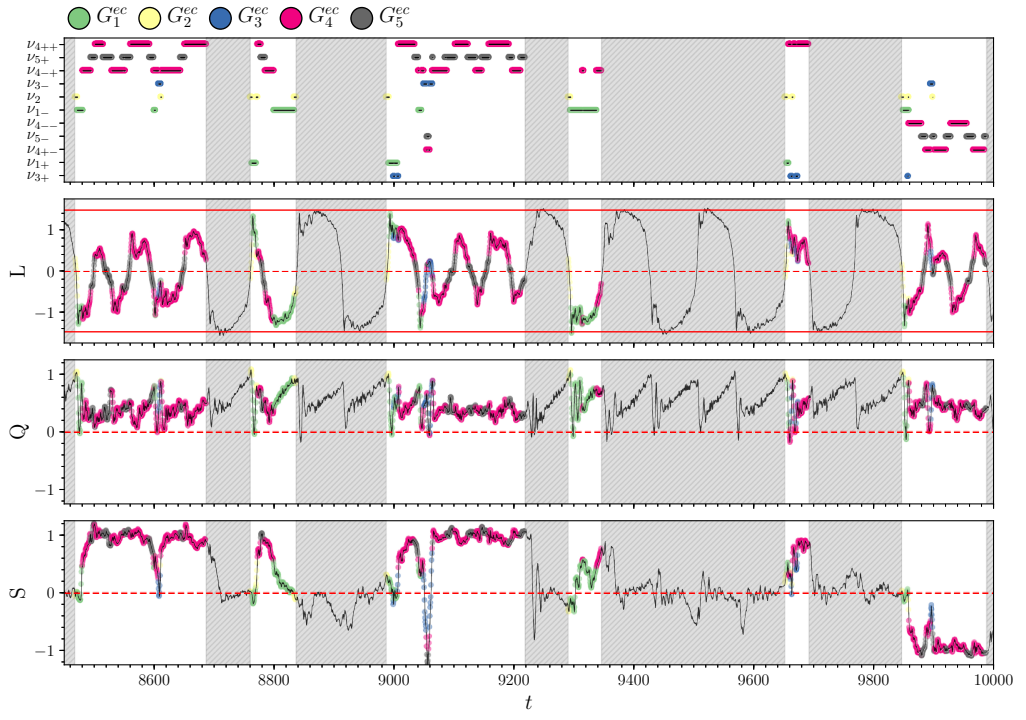

FIGURE 15. Time series indicating the cluster c_k^{ec} visited at time t and the corresponding amplitudes of modes L, Q, and S, during a series of extended cessations interspersed by several periods of consecutive flow reversals for $(Ra = 5 \cdot 10^7, Pr = 3)$. The EC subset corresponds to white areas. Data-points from the EC subset are coloured to match the groups G_k^{ec}, see colour code at the top part of the figure.

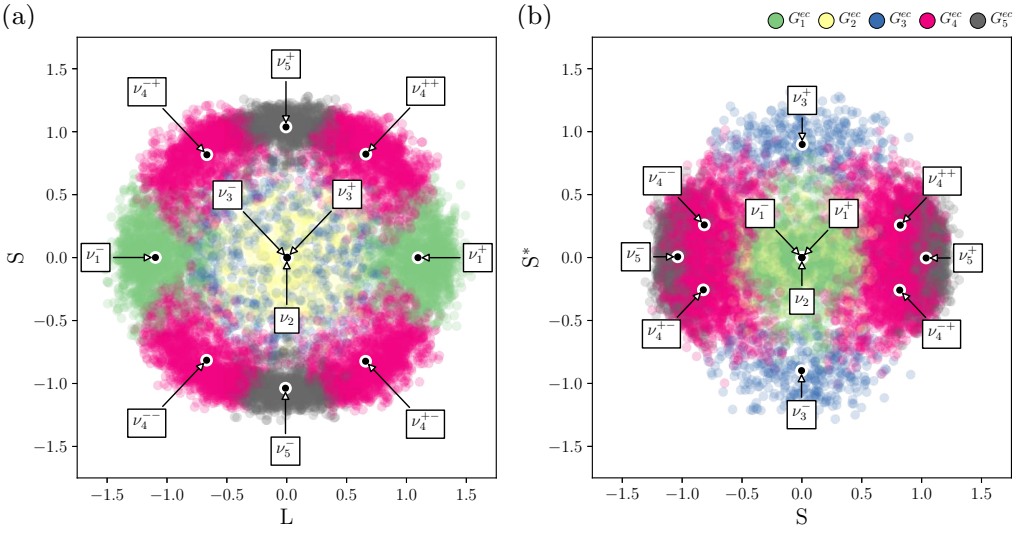

FIGURE 16. Phase diagram in the (L,S) and (L,S*) planes for $(Ra = 5 \cdot 10^7, Pr = 3)$ inside the EC subset. Colour is used to identify each cluster group, see colour code at the top of the figure: G_1^{ec}, and G_2^{ec} predominantly associated to rogue reversals, and G_3^{ec}, G_4^{ec}, and G_5^{ec} predominantly associated to extended cessations. Solid marks indicate the corresponding centroids.

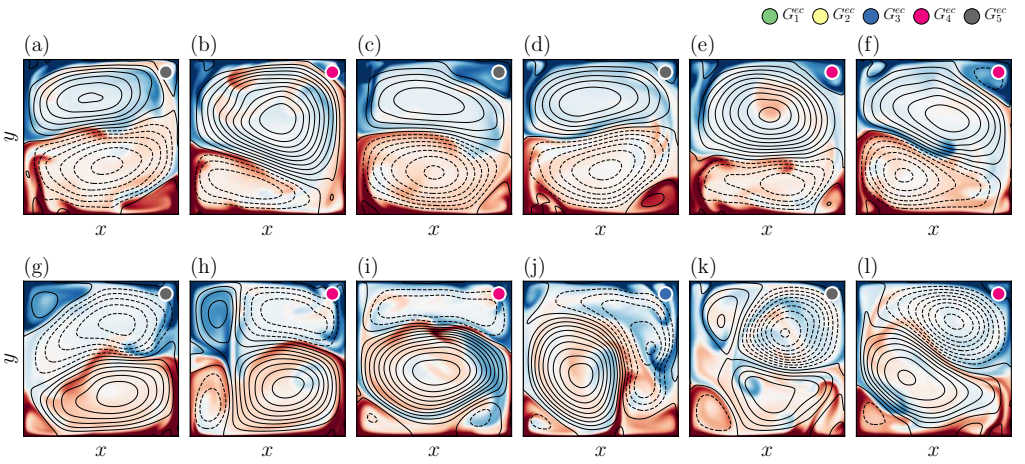

FIGURE 17. Sequence of instantaneous fields observed during actual cessations for $(Ra = 5 \cdot 10^7, Pr = 3)$. Colour indicates the temperature field $\theta(\boldsymbol{x}, t)$, lines are streamlines (negative streamfunction values in dashed). The coloured symbol of the top-right corner indicates the current cluster group (colour code at the top of the figure). Snapshots (a) to (f) are taken every 20 t.u. from $t = 9090$ to $t = 9190$, whereas snapshots (g) to (l) are taken every 4 t.u. from $t = 9882$ to $t = 9902$ illustrating a short excursion.

in mode Q and a substantial increase (of around 40%) in the global heat-transfer (not presented here). For such rapid events, the residence time is 4.6% of the total EC subset, that is less than 1% of the total simulation length (table 5b).

8. Evolution of dynamical regimes as function of Rayleigh number

For a given Pr (in practice $Pr = 4.3$ or $Pr = 3$), we take advantage of the POD and cluster-based analyses to make evidence of the dynamical flow regimes observed for different values of Ra which covers the transition from a steady-state to a turbulent flow regime. More precisely, a first study is based on the energetic content of the leading POD modes, a second on the residence time inside the different groups of clusters.

8.1. *Energy contents of leading POD modes*

To allow for a direct comparison between different Ra, we use the modes $\boldsymbol{\phi}_k$ extracted from the CR subset for $Ra = 5 \cdot 10^7$ for the Pr considered (see §4). For the different Ra, we project the instantaneous velocity and temperature fields onto the six leading POD modes $\boldsymbol{\phi}_k$ to obtain the set of amplitudes $(\alpha_k, k = 1, \cdots, 6)$. As in §5, these modal amplitudes are then scaled by a common factor which is the value $1/\overline{|\mathrm{L}|}$ for $Ra = 5 \cdot 10^7$. Afterwards we compute $\overline{\alpha_k \alpha_k}$, which is proportional to the part of the combined energy E_{comb} contained inside mode $\boldsymbol{\phi}_k$ (see section2.3). For the values of (Ra, Pr) considered, the energy contained inside the six POD modes is somewhere between 80% and 95% of the total energy E_{comb} (not presented here).

Let us focus on the energetic contents of the leading POD modes L, Q, and S (figure 18), which contain the main features of both the CR and EC regimes. As function of Ra, we may identify different dynamical regimes: below mark i mode L is dominant; between marks i and ii mode Q is dominant; above ii mode L becomes again dominant and remains so for larger values of Ra; between iii and iv mode S becomes comparable to Q; above iv mode S decreases with respect to modes L and Q. Note that, on the

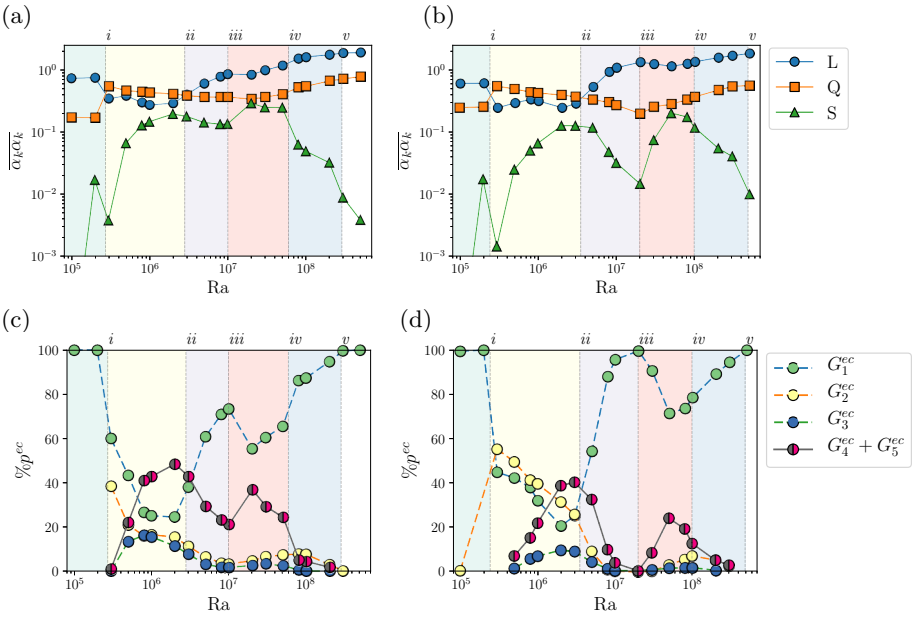

FIGURE 18. Dynamical regimes as a function of Ra for (a,c) $Pr = 3$ and (b,d) $Pr = 4.3$. Marks i to v separate the different dynamical regimes (see text). Figs. (a,b) display the rescaled values of $\overline{\alpha_k \alpha_k}$, where α_k is obtained by projection into CR modes for $Ra = 5 \cdot 10^7$. Figs. (c,d) display the probability $\%p_{ec}$ of the system being inside the cluster groups: G_1^{ec} is predominantly associated to plateaus; G_2^{ec} to transitions between plateaus; G_3^{ec} to short excursions; and G_4^{ec} and G_5^{ec} to extended cessations.

figure, we add a mark v which will be used in the next section. In the following, since both values of Pr display similar trends, we focus on the case for $Pr = 4.3$.

In order to highlight the relation between the LSC dynamics and the energetic contents of POD modes, figure 19 displays a time series of A_{2D} for different values of Ra representing each dynamical regime. For values of Ra between the onset convection and mark i, a steady-state roll is observed. The jump of mode Q around mark i coincides with the transition to unsteady flows. Region i-ii corresponds to continuous reversals of the LSC but without the accumulation phase, i.e. modes Q and L have the same dominant frequency (not presented here) and plateaus in A_{2D} are completely absent. Examples of this zone are a periodic solution like at $Ra = 3 \cdot 10^5$ (figure 19a) or when mode S becomes more energetic, chaotic reversals like at $Ra = 3 \cdot 10^6$ (figure 19b). Above mark ii, mode L becomes dominant once again. This coincides with the development of long plateaus in A_{2D}. The length of plateaus however seems to be influenced by the energetic contents of mode S. Inside region ii-iii, plateaus gradually become longer as mode S weakens (see figure 19c and number of reversals in table 2). Inside region iii-iv, as mode S becomes significant again, plateaus become shorter while the CR and EC regimes are observed intermittently (figure 19d). Finally above mark iv, as mode S weakens again, plateaus size gradually increase (figure 19e). Once mode S becomes negligible, stable plateaus are observed for as long as 2000 convective time units (figure 19f). This dependency on Ra of the flow dynamics is consistent with observations from Sugiyama *et al.* (2010) for $Pr \geqslant 4.3$ where flow reversals are observed over two discontinuous ranges of Ra. The intermediate range of Ra numbers where Sugiyama *et al.* (2010) observes no flow reversals, corresponds to the region ii-iii where flow reversals are particularly rare: for

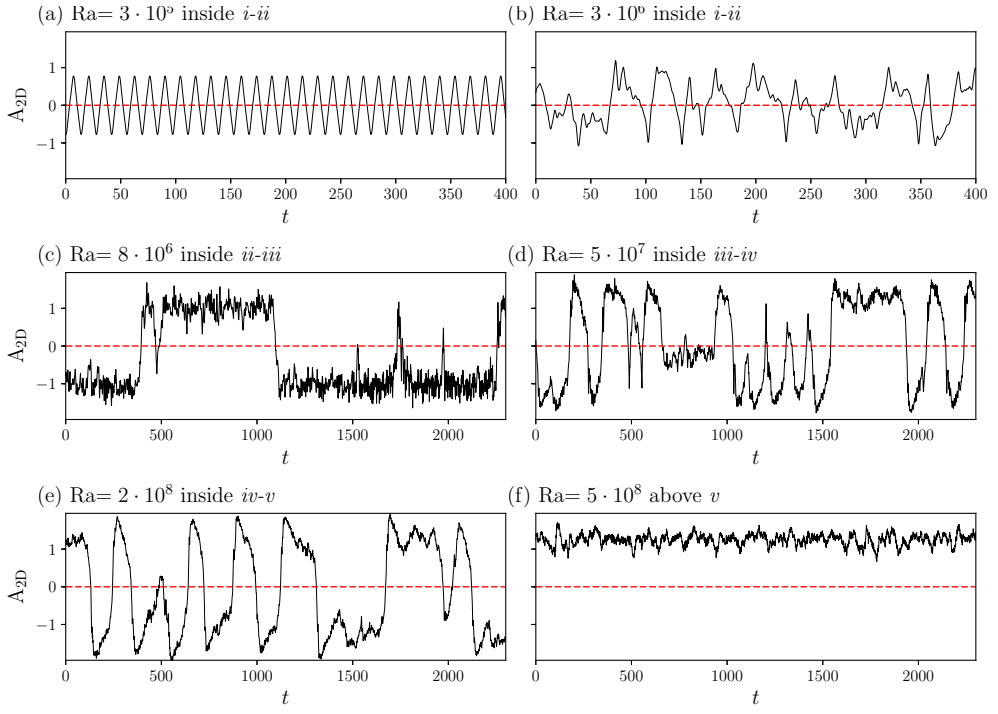

FIGURE 19. Time series of the angular impulse A_{2D} for $Pr = 4.3$ and different Ra illustrating the different flow flow regimes: (a) periodic reversals for $Ra = 3 \cdot 10^5$, (b) chaotic reversals for $Ra = 3 \cdot 10^6$, (c) presence of long plateaus for $Ra = 8 \cdot 10^6$, (d) flow reversals and extended cessations for $Ra = 5{\cdot}10^7$, (e) flow reversals for $Ra = 2{\cdot}10^8$, and (f) long plateaus for $Ra = 5{\cdot}10^8$.

instance, for $(Ra = 10^7, Pr = 4.3)$ only 3 reversals were observed over 9600 t.u. (see table 2). For this region, the waiting time between reversals can be more than 300 times larger than for the region *i-ii*.

8.2. *Residence time inside different cluster groups*

The second approach uses the cluster partitioning for each value of Pr. To allow for a direct comparison between different Ra, we use the clusters extracted from the EC subset at $Ra = 5 \cdot 10^7$. This partitioning recovers the main features of the regime of extended cessations, but also of flow reversals. For a given Ra, we assign each data-point $(\alpha_k, k = 1, \cdots, 6)$ computed in subsection 8.1 to one of the 5 groups G_k^{ec} presented in §7.1. Figure 20 displays the (L, S) phase-diagrams for the Rayleigh numbers corresponding to cases of figure 19. From this procedure, the residence time $\%p_{ec}$ of each group G_k^{ec} can be evaluated (see figure 18c for $Pr = 3$ and figure 18d for $Pr = 4.3$).

First, consider the region *i-ii*. For $Ra = 3 \cdot 10^5$, the periodic solution corresponds to a closed path along the S-axis which passes through the cluster groups G_1^{ec} and G_2^{ec} (figure 20a). Data-points inside G_1^{ec} correspond to the diagonal rolls observed during plateaus, while G_2^{ec} corresponds to the quadrupolar mode observed during the transition between positive and negative plateaus. Comparable residence times $\%p_{ec}(G_1^{ec})$ and $\%p_{ec}(G_2^{ec})$ (figure 18d) illustrate the absence of long metastable plateaus. By contrast, the chaotic reversals observed inside the same region, do not display any particular orbit and explore all of the groups (figure 20b). Accordingly, for all groups the residence time $\%p_{ec}$ has the same order between 20% and 40% (figure 18d).

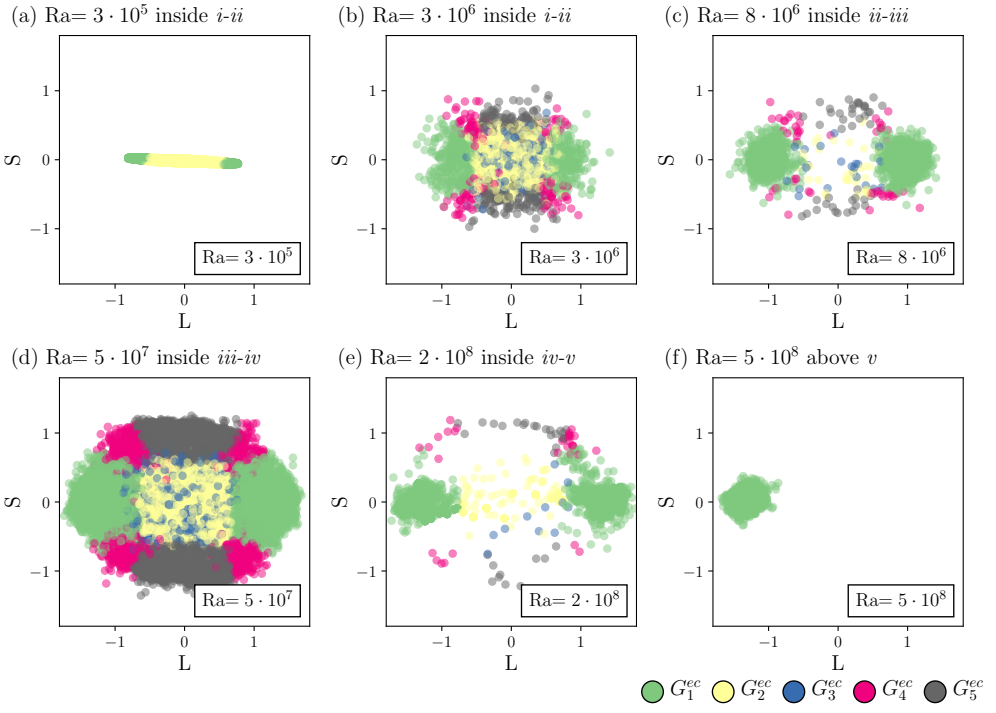

FIGURE 20. Phase diagram in the (L, S) plane for $Pr = 4.3$ and different Ra illustrating the different flow regimes presented in figure 19. Cluster groups are obtained from the EC regime for $Ra = 5 \cdot 10^7$, see colour code at the bottom of the figure: G_1^{ec} is predominantly associated to plateaus; G_2^{ec} to transitions between plateaus; G_3^{ec} to short excursions; and G_4^{ec} and G_5^{ec} to extended cessations.

Inside region *ii-iii*, G_1^{ec} becomes dominant at the expense of all the other groups, in particular of G_2^{ec}, illustrating the scarcity of flow reversals (figures 18d and 20c). Inside region *iii-iv*, the group G_1^{ec} becomes less prominent in favour of G_2^{ec} (indicating shorter plateaus), and in favour of G_4^{ec} and G_5^{ec} associated to cessation dynamics (figure 18d). The sum of residence times of G_4^{ec} and G_5^{ec} is as large as 25%, which illustrates the strong competition between the CR and EC regimes (figure 20d). Inside the region *iv-v*, G_1^{ec} and G_2^{ec} are reinforced while cessation dynamics become rare or non-existing (figures 18d and 20e). Finally, as Ra increases above *v*, groups other than G_1^{ec}, essentially disappear and only a long stable plateau is observed (figures 18d and 20f).

The sequence presented here can be compared to results from Chandra & Verma (2013) for $Pr = 1$. The ratio between the Fourier mode [2,2] (roughly equivalent to Q) and the [1,1] mode (equivalent to L) of the vertical velocity was found to decrease monotonically for Ra between $2 \cdot 10^7$ and 10^9. A similar decrease is observed inside the region *ii-iii*. However, above *iii* the ratio between modes Q and L reaches a near constant value.

9. Conclusion

In this paper we used long-term data from two-dimensional DNS of a square RB cell to extract and study the dynamics of the large-scale structures. In the range considered, intermittency between the regime of consecutive reversals (CR) and the regime of extended cessations (EC) is observed. Our approach combines a statistical approach and proper orthogonal decomposition (POD) to characterise each regime.

Initially, we split, based on a criterion depending of the global angular momentum, the overall data in two subsets, one for each flow regime. For each subset, a POD analysis is performed identifying the six most energetic large-scale flow structures. Both regimes however may be accurately represented by the same type of large-scale flow structures, suggesting that differences between the CR and EC regimes concerns, for the most part, the time evolution of these flow structures. For CR, the leading modes are centrosymmetric monopole L and quadrupole Q, while for EC, the leading mode is the symmetry-breaking vertical dipole S. For both regimes, the amplitude of the leading mode exhibits alternating positive and negative plateaus, the duration of plateaus being several times longer than the large-eddy turnover time.

A separate analysis of the probability distribution function of waiting times between reversals, suggests that the CR and EC regimes are driven by different physical processes. During the EC regime, the PDFs of waiting times for all reversing modes correspond well to exponential distribution. This seems to indicate that the system loses its memory during the EC regime. During the CR regime, PDFs of waiting times for mode L (and to a lesser extent for mode L^*) deviate much from the expected exponential distribution of a Poisson process. This observation is consistent with the energetic interpretation of the generic reversal mechanism (Castillo-Castellanos *et al.* 2016), where localised accumulation and subsequent release of thermal energy, drives the flow reversal during CR. By applying a conditional average over hundreds of realisations of particular reversals in the CR, we identified the most common dynamical features of the POD amplitudes during a generic reversal. Centrosymmetric modes $\{L, L^*, Q, Q^*\}$ are found to follow a generic cycle, whereas the symmetry-breaking modes $\{S, S^*\}$ fluctuate around zero. In this view, modes $\{S, S^*\}$ become a source of noise for a predominantly coherent dynamics. These observations are in good agreement with results from the 5-mode model by Podvin & Sergent (2017).

We also presented a simplified representation to study the long-term evolution of the large-scale structures: inside the phase-space of six leading POD amplitudes, a cluster partitioning algorithm was applied on the data set reducing the dynamics to a network of $K = 12$ or $K = 11$ states. Such a drastic approach recovered the main features of the CR regime. In addition, during the beginning of the release phase leading to the rebound event, flow reversals were shown to take one of several possible paths with equal probability. This method was then used to study the EC regime which has been much less explored. It discriminated between different dynamical events regardless of their relative timescales: weak or 'rogue' reversals and actual cessations. On the one hand, the rogue reversals deviate from standard reversals due to the intensity in mode S. On the other hand, the actual cessations are predominantly associated to a continuous push and shove motion between two vertically stacked vortices. This metastable state may be sustained for long periods of time. Moreover, sporadic reversals of this vertical dipole also have been identified during a short excursion.

As a final analysis, we combined the POD and cluster analysis to provide a description of the different spatio-temporal dynamics observed over a wide range of Rayleigh numbers. By considering the energetic content of the leading POD modes $\{L, Q, S\}$ and the residence time in each group of clusters, we were able to identify the successive dynamical regimes observed from the steady state to the turbulent regime.

As a prospective, this type of approach opens the door for a more systematic study of the transition between the regimes of consecutive flow reversals and extended cessations. A more systematic study of the dependency of the large-scale flow dynamics on the Prandtl number could also be of interest.

Acknowledgements

This work was granted access to the HPC resources of GENCI-IDRIS under allocation 2a0326 made by GENCI.

REFERENCES

Antonia, R. A. 1981 Conditional sampling in turbulence measurement. *Annual review of fluid mechanics* **13** (1), 131–156.

Arthur, D. & Vassilvitskii, S. 2007 k-means++: The advantages of careful seeding. In *Proceedings of the eighteenth annual ACM-SIAM symposium on Discrete algorithms*, pp. 1027–1035. Society for Industrial and Applied Mathematics.

Bai, K., Ji, D. & Brown, E. 2016 Ability of a low-dimensional model to predict geometry-dependent dynamics of large-scale coherent structures in turbulence. *Physical Review E* **93** (2), 023117.

Bailon-Cuba, J., Emran, M. S. & Schumacher, J. 2010 Aspect ratio dependence of heat transfer and large-scale flow in turbulent convection. *Journal of Fluid Mechanics* **655**, 152–173.

Bell, J.B., Colella, P. & Glaz, H.M. 1989 A second-order projection method for the incompressible Navier-Stokes equations. *Journal of Computational Physics* **283**, 257–283.

Brown, E. & Ahlers, G. 2007 Large-Scale Circulation Model for Turbulent Rayleigh-Bénard Convection. *Physical Review Letters* **98** (13), 134501.

Cao, Y., Kaiser, E., Borée, J., Noack, B. R., Thomas, L. & Guilain, S. 2014 Cluster-based analysis of cycle-to-cycle variations: application to internal combustion engines. *Experiments in Fluids* **55** (11), 1837.

Castillo-Castellanos, A., Sergent, A. & Rossi, M. 2016 Reversal cycle in square Rayleigh-Bénard cells in turbulent regime. *Journal of Fluid Mechanics* **808**, 614–640.

Chandra, M. & Verma, M. K. 2011 Dynamics and symmetries of flow reversals in turbulent convection. *Physical Review E* **83** (6), 067303.

Chandra, M. & Verma, M. K. 2013 Flow Reversals in Turbulent Convection via Vortex Reconnections. *Physical Review Letters* **110** (11), 114503.

Das, A., Ghosal, U. & Kumar, K. 2000 Asymmetric squares as standing waves in Rayleigh-Bénard convection. *Physical Review E* **62** (3), R3051.

Fauve, S., Herault, J., Michel, G. & Pétrélis, F. 2017 Instabilities on a turbulent background. *Journal of Statistical Mechanics: Theory and Experiment* p. 064001.

Foroozani, N., Niemela, J. J., Armenio, V. & Sreenivasan, K. R. 2017 Reorientations of the large-scale flow in turbulent convection in a cube. *Physical Review E* **95** (3), 033107.

Giannakis, D., Kolchinskaya, A., Krasnov, D. & Schumacher, J. 2018 Koopman analysis of the long-term evolution in a turbulent convection cell. *Journal of Fluid Mechanics* **847**, 735–767.

Grossmann, S. & Lohse, D. 2003 On geometry effects in Rayleigh–Bénard convection. *Journal of Fluid Mechanics* **486**, 105–114.

Holmes, P., Lumley, J. L., Berkooz, G. & Rowley, C. W. 2012 *Turbulence, Coherent Structures, Dynamical Systems and Symmetry*, 2nd edn. *Cambridge Monographs on Mechanics* . Cambridge University Press.

Horn, S. & Schmid, P. J. 2017 Prograde, retrograde, and oscillatory modes in rotating Rayleigh–Bénard convection. *Journal of Fluid Mechanics* **831**, 182–211.

Hughes, G. O., Gayen, B. & Griffiths, R. W. 2013 Available potential energy in Rayleigh-Bénard convection. *Journal of Fluid Mechanics* **729**, R3.

Hussain, A.K.M. F. 1986 Coherent structures and turbulence. *Journal of Fluid Mechanics* **173**, 303–356.

Jain, A. K. 2010 Data clustering: 50 years beyond k-means. *Pattern Recognition Letters* **31** (8), 651 – 666.

Kadanoff, L. P. 2001 Turbulent heat flow: Structures and scaling. *Physics today* **54** (8), 34–39.

Kaiser, E., Noack, B. R., Cordier, L., Spohn, A., Segond, M., Abel, M., Daviller, G., sth, J., Krajnovi, S. & Niven, R. K. 2014 Cluster-based reduced-order modelling of a mixing layer. *Journal of Fluid Mechanics* **754**, 365–414.

Lhuillier, F., Hulot, G. & Gallet, Y. 2013 Statistical properties of reversals and chrons in numerical dynamos and implications for the geodynamo. *Physics of the Earth and Planetary Interiors* **220**, 19–36.

McFadden, P.L. & Merrill, R.T. 1986 Geodynamo energy source constraints from palaeomagnetic data. *Physics of the Earth and Planetary Interiors* **43** (1), 22 – 33.

Merrill, R., McElhinny, M. & McFadden, P. 1998 Chapter five reversals of the earth's magnetic field. In *The Magnetic Field of the Earth: Paleomagnetism, the Core, and the Deep Mantle*, *International Geophysics*, vol. 63, pp. 163 – 215. Academic Press.

Molenaar, D., Clercx, H. J. H. & Van Heijst, G. J. F. 2004 Angular momentum of forced 2D turbulence in a square no-slip domain. *Physica D: Nonlinear Phenomena* **196**, 329–340.

Ni, R., Huang, S.-D. & Xia, K.-Q. 2015 Reversals of the large-scale circulation in quasi-2D Rayleigh–Bénard convection. *Journal of Fluid Mechanics* **778**, R5.

Niemela, J.J., Skrbek, L., Sreenivasan, K.R. & Donnelly, R.J. 2001 The wind in confined thermal convection. *Journal of Fluid Mechanics* **449**, 169–178.

Pedregosa, F., Varoquaux, G., Gramfort, A., Michel, V., Thirion, B., Grisel, O., Blondel, M., Prettenhofer, P., Weiss, R., Dubourg, V., Vanderplas, J., Passos, A., Cournapeau, D., Brucher, M., Perrot, M. & Duchesnay, E. 2011 Scikit-learn: Machine learning in Python. *Journal of Machine Learning Research* **12**, 2825–2830.

Petschel, K., Wilczek, M., Breuer, M., Friedrich, R. & Hansen, U. 2011 Statistical analysis of global wind dynamics in vigorous Rayleigh-Bénard convection. *Physical Review E* **84** (2), 026309.

Podvin, B. & Sergent, A. 2015 A large-scale investigation of wind reversal in a square Rayleigh-Bénard cell. *Journal of Fluid Mechanics* **766**, 172–201.

Podvin, B. & Sergent, A. 2017 Precursor for wind reversal in a square Rayleigh-Bénard cell. *Physical Review E* **95** (1), 013112.

van der Poel, E. P., Stevens, R.J.A.M. & Lohse, D. 2011 Connecting flow structures and heat flux in turbulent Rayleigh-Bénard convection. *Physical Review E* **84** (4), 045303.

Popinet, S. 2003 Gerris: a tree-based adaptive solver for the incompressible euler equations in complex geometries. *Journal of Computational Physics* **190** (2), 572–600.

Popinet, S. 2009 An accurate adaptive solver for surface-tension-driven interfacial flows. *Journal of Computational Physics* **228** (16), 5838–5866.

Popinet, S. 2015 A quadtree-adaptive multigrid solver for the Serre–Green–Naghdi equations. *Journal of Computational Physics* **302**, 336–358.

Schmid, P. J. 2010 Dynamic mode decomposition of numerical and experimental data. *Journal of fluid mechanics* **656**, 5–28.

Shraiman, B. I. & Siggia, E. D. 1990 Heat transport in high-Rayleigh-number convection. *Physical Review A* **42** (6), 3650–3653.

Sirovich, L. 1987 Turbulence and the dynamics of coherent structures part I: coherent structures. *Quarterly of applied mathematics* **45** (3), 561–571.

Sreenivasan, K. R., Bershadskii, A. & Niemela, J.J. 2002 Mean wind and its reversal in thermal convection. *Physical Review E* **65** (5), 056306.

Sugiyama, K., Ni, R., Stevens, R.J.A.M., Chan, T. S., Zhou, S.-Q., Xi, H.-D., Sun, C., Grossmann, S., Xia, K.-Q. & Lohse, D. 2010 Flow reversals in thermally driven turbulence. *Physical Review Letters* **105** (3), 034503.

Valet, J.-P., Fournier, A., Courtillot, V. & Herrero-Bervera, E. 2012 Dynamical similarity of geomagnetic field reversals. *Nature* **490** (7418), 89–93.

Van Heijst, G. J. F., Clercx, H. J. H. & Molenaar, D. 2006 The effects of solid boundaries on confined two-dimensional turbulence. *Journal of Fluid Mechanics* **554**, 411–431.

Vasilev, A. Y. & Frick, P. G. 2011 Reversals of large-scale circulation in turbulent convection in rectangular cavities. *JETP letters* **93** (6), 330–334.

Wicht, J., Stellmach, S. & Harder, H. 2009 *Numerical Models of the Geodynamo: From Fundamental Cartesian Models to 3D Simulations of Field Reversals*, pp. 107–158. Berlin, Heidelberg: Springer Berlin Heidelberg.

Winters, K. B., Lombard, P. N., Riley, J. J. & D'Asaro, E. A. 1995 Available potential energy and mixing in density-stratified fluids. *Journal of Fluid Mechanics* **289**, 115–128.

Xi, H.-D. & Xia, K.-Q. 2008*a* Azimuthal motion, reorientation, cessation, and reversal of the

large-scale circulation in turbulent thermal convection: A comparative study in aspect ratio one and one-half geometries. *Physical Review E* **78** (3), 036326.

Xi, H.-D. & Xia, K.-Q. 2008*b* Flow mode transitions in turbulent thermal convection. *Physics of Fluids* **20** (5), 055104.